Title

Measurement of Surface-Wave Phase-Velocity Dispersion on Mixed Inertial Seismometer – Distributed Acoustic Sensing Seismic Noise Cross-Correlations

Journal

Bulletin of the Seismological Society of America, 111(6)

ISSN

0037-1106

Authors

Nayak, Avinash
Ajo-Franklin, Jonathan

Publication Date

2021-12-01

DOI

10.1785/0120210028

Peer reviewed

Measurement of Surface-Wave Phase Velocity Dispersion on Mixed Inertial Seismometer - Distributed Acoustic Sensing Seismic Noise Cross-Correlations

by Avinash Nayak[1*], Jonathan Ajo-Franklin[1,2], Imperial Valley Dark Fiber Team

May 12, 2021

For submission to BSSA

[1]Earth and Environmental Science Area, Lawrence Berkeley National Laboratory, Berkeley, CA, USA

[2]Department of Earth, Environmental, and Planetary Sciences, Rice University, Houston, TX, USA

Corresponding author: Avinash Nayak, anayak7@lbl.gov

1 Cyclotron Road, LBNL M/S 74R316C, Berkeley, CA 94720, USA.

Jonathan Ajo-Franklin, ja62@rice.edu

Imperial Valley Dark Fiber Team,

Representative: Jonathan Ajo-Franklin, darkfiberdas@gmail.com

Declaration of Competing Interests

The authors acknowledge there are no conflicts of interest recorded.

Abstract The application of ambient seismic noise cross correlation to distributed acoustic sensing (DAS) data recorded by subsurface fiber-optic cables has revolutionized our ability to obtain high resolution seismic images of the shallow subsurface. However, passive surface-wave imaging using DAS arrays is often restricted to Rayleigh-wave imaging and 2D imaging along straight segments of DAS arrays due to the intrinsic sensitivity of DAS being limited to axial strain along the cable for the most common type of fiber. We develop the concept of estimating empirical surface waves from mixed-sensor cross-correlation of velocity noise recorded by three-component seismometers and strain-rate noise recorded by DAS arrays. Using conceptual arguments and synthetic tests, we demonstrate that these cross-correlations converge to empirical surface-wave axial strain response at the DAS arrays for virtual single step forces applied at the seismometers. Rotating the three orthogonal components of the seismometer to a tangential-radial-vertical reference frame with respect to each DAS channel permits separate analysis of Rayleigh waves and Love waves for a medium that is sufficiently close to 1D and isotropic. We also develop and validate expressions that facilitate the measurement of surface-wave phase velocity on these noise cross-correlations at far-field distances using frequency-time analysis. These expressions can also be used for DAS surface-wave records of active sources at local distances. We demonstrate the recovery of both Rayleigh waves and Love waves in noise cross-correlations derived from a dark fiber DAS array in the Sacramento basin, Northern California and nearby permanent seismic stations at frequencies $\sim$0.1-0.2 Hz, up to distances of $\sim$80 km. The phase velocity dispersion measured on these noise cross-correlations are consistent with those measured on traditional noise cross-correlations for seismometer pairs. Our results extend the application of DAS to 3D ambient noise Rayleigh-wave and Love-wave tomography using seismometers surrounding a DAS array.

Introduction

The retrieval of empirical Green's functions from cross-correlation of diffused seismic wavefields recorded at pairs of seismometers, primarily ambient seismic noise, led to a major advancement in surface-wave tomography at local and regional scales, especially in the absence of active sources and earthquakes (Shapiro and Campillo, 2004; Shapiro *et al.*, 2005; Yao *et al.*, 2006; Lin *et al.*, 2008; Lin *et al.*, 2013; Lin *et al.*, 2014; Nayak *et al.*, 2020). The resolution is primarily controlled by the frequency content of background seismic noise (natural or anthropogenic) and station spacing, which can be a few tens of km for permanent regional seismic networks (Nishida *et al.*, 2008) and as low as $\sim$10 m for short-term ($\sim$1 month) dense nodal deployments over small areas (Roux *et al.*, 2016). Application of noise cross-correlation to distributed acoustic sensing (DAS) data has revolutionized our ability to obtain high resolution seismic images of the shallow subsurface, particularly for subsurface monitoring and geotechnical surveys in urban areas (Dou *et al.*, 2017; Martin *et al.*, 2017; Zeng *et al.*, 2017; Zeng *et al.*, 2017; Martin and Biondi, 2018; Ajo-Franklin *et al.*, 2019). DAS is a technology that transforms low-cost fiber-optic cables used in telecommunication, usually buried a few meters under the ground, into a linear array of sensors measuring strain or strain rate by applying coherent optical time domain reflectometry to detect changes in Rayleigh scattering induced by extensional strain (Hartog, 2017). DAS can provide dense, wide bandwidth, and continuous long-duration seismic recordings with spatial resolutions of a few meters over distances of a few tens of kilometers (Daley *et al.*, 2013; Daley *et al.*, 2016), which can be used for noise cross-correlation and high-resolution surface-wave imaging. Extensive pre-existing networks of unused subsurface fiber-optic cables known as dark fiber can also be used for this purpose (Jousset *et al.*, 2018; Martin and Biondi, 2018; Ajo-Franklin *et al.*, 2019; Wang *et al.*, 2020; Karrenbach *et al.*, 2020; Zhu *et al.*, 2021).

The cross-correlation of seismic noise recorded at two three-component inertial seismometers yields a nine-component empirical Green's tensor. In this study, we denote the components of empirical Green's tensor in the Tangential (T)-Radial (R)-Vertical (Z) reference frame as TR, ZT, etc., in which the first and the second letters are the single force direction and the corresponding direction of motion at the source and the receiver sensors, respectively. A pair of three-component seismometers can provide both Rayleigh wave and Love wave information - Rayleigh waves on the four components in the radial-vertical plane (components RR, RZ, ZR, ZZ; hereinafter referred to as the [R/Z] components), and Love waves on the TT component (Nishida *et al*., 2008; Lin *et al*., 2008; Lin *et al*., 2014; Nayak *et al*., 2018; Nayak *et al*., 2020). In contrast, the most common geometry of fiber used in DAS is only sensitive to axial strain in the direction of the fiber-optic cable and there is only one component (Kuvshinov, 2016). While helical and more complicated fiber geometries (Mateeva *et al*., 2014; Kuvshinov, 2016; Ning and Sava, 2018) have been proposed with distinct sensitivities, use of the existing telecommunication installation limits us to measurement of a single strain component. For horizontal DAS arrays, cross-correlation of radial strain noise recorded by channels in a straight fiber segment returns Rayleigh waves (Dou *et al*., 2017; Martin *et al*., 2017; Zeng *et al*., 2017; Zeng *et al*., 2017; Martin and Biondi, 2018; Ajo-Franklin *et al*., 2019). Cross-correlation of strain recorded by channels that are not in a straight line or by DAS array segments of different orientation typically yields a mixture of Rayleigh and Love waves (Martin *et al*., 2017; Luo *et al*., 2020; Song *et al*., 2021) that may be difficult to interpret. Retrieval of pure Love waves in noise cross-correlations involving DAS data only is difficult due to the transverse polarization of Love waves and the intrinsic radial sensitivity of DAS (Martin *et al*., 2018). Therefore, noise cross-correlation and surface-wave imaging using DAS arrays are often restricted to Rayleigh-wave imaging and 2D imaging along straight segments of DAS arrays.

In many regions, dark fiber networks are surrounded by regional seismic stations (Lindsey *et al*., 2017; Yu *et al*., 2019). Dense temporary networks of seismometers may also be deployed along with DAS arrays for active-source surveys (Parker *et al*., 2018). When both resources are present, the integration of DAS with existing seismological networks might have distinct advantages in terms of spatial resolution and coverage. In this study, we analyze the surface waves retrieved from mixed-sensor noise cross-correlations involving inertial seismometers and horizontal DAS arrays. First, we derive expressions for the phase of surface-wave axial strain in an arbitrary direction with respect to the wave propagation direction in the cylindrical coordinate system. This permits measurement of surface-wave phase velocity on a single channel of a DAS array at local distances for active, passive or virtual sources placed at any backazimuth with respect to the DAS array. The expressions are verified by measuring phase velocity on synthetic waveforms using automatic frequency-time analysis (AFTAN) (Bensen *et al.*, 2007; Lin *et al.*, 2008). Then we perform synthetic tests to analyze the cross-correlations involving synthetic velocity noise recorded by three-component inertial seismometers as virtual sources and synthetic strain-rate noise recorded by the channels of a DAS array as virtual receivers, for a homogeneous ambient noise source distribution. These noise cross-correlations converge to the empirical strain response of the medium at the DAS array for single step forces applied at the seismometer. The three components of a seismometer, i.e. the single force directions at the virtual source, can be rotated to the T-R-Z reference frame with respect to each DAS channel. For an isotropic and 1D medium, we demonstrate that the empirical strain response of DAS retrieved from these noise cross-correlations corresponds to pure Rayleigh wave for a radial and vertical source, and pure Love wave for a tangential source. Using the expressions derived for the phase of surface-wave axial strain in an arbitrary direction, we successfully measure Rayleigh-wave and Love-wave phase velocity dispersion on the synthetic mixed-sensor noise cross-correlations. Then we demonstrate recovery of surface waves in noise cross-correlations derived from real data recorded by a dark fiber DAS array in the Sacramento basin, Northern California (Ajo-Franklin *et al.*, 2019) and nearby permanent seismic stations in the secondary microseism passband ($\sim$0.1-0.2 Hz) up to distances of $\sim$80 km. Using the same seismometer as a virtual source, we find the Rayleigh-wave and Love-wave phase velocity dispersion measured on mixed sensor noise cross-correlations for a particular DAS channel to be consistent with those measured on traditional seismometer-seismometer noise cross-correlations for a seismometer collocated with the DAS channel. Our results extend the application of DAS to 3D surface-wave tomography and to both Rayleigh-wave and Love-wave tomography. Active sources can be used at local distances and ambient noise cross-correlations can be used at both local and regional distances.

Phase of surface-wave axial strain in an arbitrary direction

We restrict this study to axial strain in the horizontal plane and horizontal DAS arrays, most relevant to surface fiber installation. Measurement of two-point (from a source to a receiver) phase velocity on surface-wave records involves measurement of the complex phase using frequency-time analysis (Bensen *et al.*, 2007; Lin *et al.*, 2008). We first derive the expressions for the complex phase of surface-wave axial strain at an arbitrary direction with respect to the wave propagation direction. This permits measurement of phase or phase velocity on a single axial strain record for a source placed at any backazimuth. For sources located in line with a DAS array, multi-channel methods such as Multi-Channel Analysis of Surface Wave (MASW) or Frequency-Wavenumber (FK) analysis can be conveniently used to measure the phase velocity dispersion (Dou *et al.*, 2017; Zeng *et al.*, 2017; Ajo-Franklin *et al.*, 2019). A plane-wave approximation is also commonly assumed for interpreting body-wave and surface-wave records of distant earthquakes on DAS arrays (Lindsey *et al.*, 2017; Wang *et al.*, 2018; Yu *et al.*, 2019). Instead, we adopt a cylindrical coordinate system for horizontally propagating surface waves in an isotropic 1D medium at local and regional distances (Aki and Richards, 2002). The far-field surface-wave time series $u(r,t)$ can be expressed as the inverse Fourier transform of a kernel $U(\omega, r)$.

$$
\begin{aligned}
u(r,t) &= \frac{1}{2\pi}\int_{-\infty}^{\infty} U(\omega, r) e^{-i\omega t}\, d\omega \\
U(\omega, r) &= A(\omega, r) e^{ikr+i\phi_0}
\end{aligned}
\quad (1)
$$

where r, t, ω and k are distance, time, angular frequency, and wavenumber, respectively; ϕ_0 is an initial phase term, and A is an amplitude factor. k and the phase velocity c are related by $kc = \omega$. ϕ_0 is an integral multiple of $\pm\frac{\pi}{4}$ for surface-wave empirical Green's functions retrieved from multi-component noise cross-correlations (Aki and Richards, 2002). The sign convention of the Fourier transform in equation (1) is the same as in Bensen *et al.* (2007) and Lin *et al.* (2008), and is different from Herrmann (2014). Hereinafter, intrinsic dependencies of U and A on ω and r are omitted for the sake of notational simplicity. Figure 1a shows the geometry. Assuming the direction of propagation is at an angle ψ with respect to the $+x$ direction, Rayleigh-wave particle displacement $\overrightarrow{U_{LR}}$ is in the radial direction $(\cos\psi, \sin\psi)$ in the horizontal plane (x, y).

$$\overrightarrow{U_{LR}} = A(\cos\psi, \sin\psi)e^{ikr+i\phi_0} \tag{2}$$

We can transform equation (2) into Cartesian coordinates using $\cos\psi = \frac{x}{\sqrt{x^2+y^2}}$, $\sin\psi = \frac{y}{\sqrt{x^2+y^2}}$, and $r = \sqrt{x^2+y^2}$. Following Martin *et al.* (2018), for a displacement wavefield $\overrightarrow{u} = (u_x, u_y)$, the axial strain ε in an arbitrary direction at an angle φ with respect to the $+x$ direction is obtained through tensor rotation (Bower, A. F., 2010, Applied Mechanics of Solids, Appendix D, `http://solidmechanics.org/`, last accessed April 2021).

$$\varepsilon = (\cos^2\varphi)\frac{\partial u_x}{\partial x} + (\cos\varphi)(\sin\varphi)(\frac{\partial u_x}{\partial y} + \frac{\partial u_y}{\partial x}) + (\sin^2\varphi)\frac{\partial u_y}{\partial y} \tag{3}$$

We denote the angle between the direction of propagation $\hat{\psi}$ and the direction in which we wish to calculate axial strain $\hat{\varphi}$ by θ. Applying equation (3) to equation (2) and replacing $(\psi - \varphi)$ by θ, it can be shown that Rayleigh-wave axial strain at an angle θ with respect to the direction of propagation is given by

$$\varepsilon_{\theta,LR} = A\left(\frac{\nabla A.\hat{\varphi}}{A}\cos\theta + \frac{\sin^2\theta}{r} + ik\cos^2\theta\right)e^{ikr+i\phi_0} \tag{4}$$

The detailed derivation is provided in the electronic supplement. $\nabla A.\hat{\varphi}$ in the first term is the directional derivative of surface-wave amplitude along the direction $\hat{\varphi}$. We assume the generic form of geometrical spreading for surface waves $A = \frac{A_0}{\sqrt{r}}$, in which A_0 is a constant and neglect anelastic attenuation.

$$\frac{\nabla A.\hat{\varphi}}{A} = -\frac{\cos\theta}{2r} \tag{5}$$

Simplifying,

$$\varepsilon_{\theta,LR} = \frac{A\cos^2\theta}{r}(-0.5 + \tan^2\theta + ikr)e^{ikr+i\phi_0} \tag{6}$$

Both Rayleigh-wave displacement and strain are zero at an angle normal to the direction of propagation ($\theta = 90°$). Collecting terms that modulate the complex phase of the strain wavefield,

$$\varepsilon_{\theta,LR} = A' e^{i(kr+\phi')+i\phi_0}$$

$$\phi' = \text{atan2}(kr, (-0.5 + \tan^2\theta)) = \text{atan2}(2\pi(r/\lambda), (-0.5 + \tan^2\theta))$$

$$A' = \frac{A\cos^2\theta}{r}\sqrt{(-0.5 + \tan^2\theta)^2 + k^2r^2} \tag{7}$$

A' is a modified amplitude term. ϕ' is an additional phase correction term that must be used for correct measurement of Rayleigh-wave phase velocity on a single axial strain record using frequency-time analysis. In case of plane-wave approximation (e.g. (Blum *et al.*, 2010)), A can be assumed to be a constant and $r \gg \lambda$. Equation (4) reduces to

$$\varepsilon_{\theta,LR,pw} = Aik(\cos^2\theta)e^{ikr+i\phi_0} = Ak(\cos^2\theta)e^{i(kr+\frac{\pi}{2})+i\phi_0}$$

$$\phi'_{pw} = \frac{\pi}{2} \tag{8}$$

The subscript pw in equation (8) denotes plane-wave approximation. In equation (7), the imaginary term kr is essentially 2π times the number of wavelengths traveled (r/λ). At large distances that are equivalent to large number of wavelengths, ϕ' is nearly equal to $\frac{\pi}{2}$ which is the phase shift obtained for plane-wave approximation. Additionally, at a fixed distance, the phase correction term is more important for longer periods than for shorter periods. ϕ' is the same for the angles θ,$-\theta$ and $(180° - \theta)$ due to the periodicity and squared value of the tangent function.

Similarly, Love-wave particle displacement $\overrightarrow{U_{LQ}}$ is in the tangential direction $(\sin\psi, -\cos\psi)$.

$$\overrightarrow{U_{LQ}} = A(\sin\psi, -\cos\psi)e^{ikr+i\phi_0} \tag{9}$$

Note that A is here is different from that for Rayleigh waves, the subscripts are omitted for the sake of notational simplicity as we are primarily interested in the phase. Solving in a similar fashion (detailed derivation in the electronic supplement), Love-wave axial strain at an angle θ with respect to the direction of propagation is given by

$$\varepsilon_{\theta,LQ} = \left((\nabla A.\hat{\varphi}) \sin\theta + \frac{A}{2}(\sin 2\theta)\left(\frac{-1}{r} + ik\right)\right) e^{ikr+i\phi_0} \tag{10}$$

Again approximating the amplitude decay by surface-wave geometrical spreading only,

$$\varepsilon_{\theta,LQ} = \frac{A}{2r}(\sin 2\theta)(-1.5 + ikr)e^{ikr+i\phi_0} \tag{11}$$

Love wave strains are identically zero in both the radial direction with respect to the direction of propagation ($\theta = 0°$; the Love wave displacement is also zero) and also normal to the direction of propagation ($\theta = 90°$; while the Love-wave displacement is maximum, the strain is zero). Equation (11) also predicts polarity reversal of waveforms at $\theta = 90°$. Collecting terms that modulate the complex phase of the strain wavefield,

$$\varepsilon_{\theta,LQ} = A' e^{i(kr+\phi')+i\phi_0}$$

$$\phi' = \text{atan2}(kr \sin 2\theta, -1.5 \sin 2\theta) = \text{atan2}(2\pi(r/\lambda) \sin 2\theta, -1.5 \sin 2\theta)$$

$$A' = \frac{A}{2r}(\sin 2\theta)\sqrt{2.25 + k^2 r^2} \tag{12}$$

The phase correction term ϕ' must be used for correct measurement of Love-wave phase velocity on a single axial strain record using frequency-time analysis. The $\sin 2\theta$ term is present in both the real and imaginary component, and controls the sign or the phase quadrant of ϕ'. Whereas ϕ' for Rayleigh waves is a continuously varying function of θ, ϕ' for Love waves depends only on the sign of $\sin 2\theta$ and can take only two possible values for a given period and distance, atan2(kr,-1.5) or atan2($-kr$,1.5). In case of plane-wave approximation, equation (10) reduces to

$$
\begin{aligned}
\varepsilon_{\theta,LQ,pw} &= 0.5Aik(\sin 2\theta)e^{ikr+i\phi_0} \\
\phi'_{pw} &= \frac{\pi}{2}\mathrm{sgn}(\sin 2\theta)
\end{aligned} \tag{13}
$$

Equations (7) and (12) can be used to measure surface-wave phase velocity on a single record of axial strain in an arbitrary direction for single force sources at distances in which far-field surface-wave approximation is valid (generally, $r \gtrsim \lambda$; (Lin *et al.*, 2013)). Both virtual sources such as velocity noise records of inertial seismometers when cross-correlated with strain-rate records of noise (see the following section) and active sources such as vibroseis acting in radial, transverse or vertical vibration modes (Parker *et al.*, 2018) can be used. The strain records could be from a strainmeter (Gomberg and Agnew, 1996) or from DAS. While DAS measures a weighted average of strain (or strain rate) over a gauge length, measurement from DAS is expected to be close to a point axial strain measurement for wavelengths much longer than a gauge length (Martin *et al.*, 2018). For earthquakes, the initial phase ϕ_0 is a function of source depth, source-receiver azimuth, focal mechanism, source-time function and elastic properties at the source (Ekström *et al.*, 1997) and must be accounted for phase velocity measurement on a single record.

We also examine the error in the measured phase velocity caused by plane-wave approximation (equations 8 and 13). Assuming the correct phase velocity and phase correction factor are c and ϕ', respectively, and the corresponding quantities for plane-wave approximation are c_{pw} and ϕ'_{pw}, respectively, the measured phase can be expressed as,

$$
\begin{aligned}
\frac{\omega r}{c} + \phi' &= \frac{\omega r}{c_{pw}} + \phi'_{pw} \\
\frac{c_{pw} - c}{c} &= \frac{\phi'_{pw} - \phi'}{2\pi(r/\lambda) - \phi'_{pw} + \phi'}
\end{aligned} \tag{14}
$$

The relative error can be calculated by plugging in the expressions for ϕ' and ϕ'_{pw} from equations 7 and 8, respectively, for Rayleigh waves and equations 12 and 13, respectively, for Love waves. The relative error is a function of θ and the distance travelled in terms of the number of wavelengths (r/λ) for Rayleigh waves and only a function of r/λ for Love waves, and is plotted in Figure S1. Phase velocity measurements from noise cross-correlations are usually restricted to interstation distances $r \gtrsim 2\lambda - 3\lambda$ to avoid bias at shorter distances caused by inhomogeneous noise source distributions (Lin *et al.*, 2008; Lin *et al.*, 2014). The error in Rayleigh-wave phase velocity is $\lesssim 0.4\%$ for distances $\gtrsim 2\lambda$ and $\theta \lesssim 45°$ (Figure S1a). The errors are zero for $\theta \sim 35.26°$ ($\tan^2\theta = 0.5$), are positive (measured phase velocity > true phase velocity) for $\theta > 35.26°$, and are negative for $\theta < 35.26°$. For Love waves, the measured phase velocity is always less than the true phase velocity and the error is $\lesssim 0.4\%$ for distances $\gtrsim 3\lambda$ (Figure S1b). For high precision tomography or for dispersion measurements at smaller distances (for example, with active source data), the errors are larger and the general phase correction factors should be used (equations 7 and 12).

To validate these expressions, we measure phase velocity on fundamental mode surface-wave synthetic strain waveforms calculated using the California Central Coast Ranges 1-D velocity model, GIL7 (Stidham *et al.*, 1999) and the modal summation method, as provided in Herrmann (2013). We arrange five receivers at 2 m spacing (h in equation 15) along the x axis centered at the origin (Figure 1b,c); the four outermost receivers are used to calculate strain at the central receiver. The sources are distributed in concentric circles of radii 30:10:90 km and at angular spacing $10°$. We calculate the displacement response along the $+x$ direction for single forces acting in the radial, tangential and vertical directions with respect to each receiver. The waveforms, originally sampled at 20 Hz, are bandpass filtered between 0.05-1.0 Hz by applying quarter-cycle-cosine tapers in the frequency domain at the two corner periods. The axial strain in the $+x$ direction at the central receiver is calculated by a 4th order accurate central-difference operator on the displacements at the four neighboring receivers, followed by decimation to 10 Hz.

$$\varepsilon_{xx}(x=0, y=0) = \frac{-u_x(2h,0) + 8u_x(h,0) - 8u_x(-h,0) + u_x(-2h,0)}{12h} \tag{15}$$

We modified the original AFTAN method (Bensen *et al.*, 2007; Lin *et al.*, 2008) to incorporate the phase correction factors ϕ'.

$$\phi(t_{max}) = kr - \omega t_{max} + \phi_0 + 2\pi N + \phi'(kr, \theta) \tag{16}$$

$\phi(t_{max})$ is the phase measured at the group arrival time t_{max}. Since equation (16) is non-linear, we solve for $c = \frac{\omega}{k}$ using grid search in the range of -30% to +30% around the reference value at each period. The reference dispersion curve, which is used to estimate the value of N, is assumed to be the synthetic dispersion curve for the actual velocity model. Similar to noise cross-correlations, we impose a minimum distance criterion on phase velocity measurements ($r \geq 2.1\lambda$).

We measure Rayleigh-wave and Love-wave dispersion on strain records for vertical and tangential forces, respectively. Figure 2 shows the results. Incorporating the general phase correction factor ϕ' (equations 7 and 12) leads to correct dispersion measurements (Figure 2a,c). We also examine the errors in the dispersion measurements upon applying plane-wave approximation (equations 8 and 13). As expected, the errors in Rayleigh-wave phase velocity dispersion measurements are greater at longer periods and vary smoothly with θ (Figure 2b). The errors are $\lesssim 1.0\%$ for $\theta \lesssim 50°$ at these distances and periods typically used in noise cross-correlation tomography ($r \geq 2.1\lambda$ in this study). In the infrastructure frequency range, for example at ~5 Hz, typical phase velocities from other DAS studies are ~300-500 m/s (Dou *et al.*, 2017; Zeng *et al.*, 2017; Ajo-Franklin *et al.*, 2019), which necessitates distances $\gtrsim$ 120-200 m and $\theta \lesssim 55°$ for errors $\lesssim 1.0\%$. While the general phase correction factor leads to correct measurements at $\theta \gtrsim 60°$, practical recovery of reliable measurements could be difficult due to decreasing amplitudes of Rayleigh waves and the effect of 3D velocity structure, as we show in the following discussions. For Love waves, the errors are $\lesssim 1.0\%$ at these distances and periods for all θ (Figure 2d).

Ambient Noise Cross-Correlations between Inertial Seismometers and DAS

In this study, we assume that ambient noise sources are uniformly distributed over Earth's surface. We refer readers to (Paitz *et al.*, 2019) for a more detailed discussion of noise cross-correlations involving DAS data for an inhomogeneous noise source distribution. The cross-correlation of components i, j of velocity v recorded at sensors A, B at locations $\boldsymbol{x}_A$, $\boldsymbol{x}_B$, respectively, in the frequency domain (Prieto *et al.*, 2011; Nayak *et al.*, 2018) can be written as

$$\langle v_i^*(\boldsymbol{x}_A, \omega) v_j(\boldsymbol{x}_B, \omega)\rangle \propto -G_{ij}(\boldsymbol{x}_A, \boldsymbol{x}_B, \omega) \tag{17}$$

$G_{ij}(\boldsymbol{x}_A, \boldsymbol{x}_B, \omega)$ is the j^{th} component of displacement at virtual receiver B in response to an input single step force in direction i at virtual source A. $\langle\rangle$ implies stacking results for data recorded over multiple time windows known as ensemble averaging. The velocity records are usually spectrally whitened prior to calculating the cross-spectrum to reduce the effect of non-flat nature of the ambient seismic field (Bensen *et al.*, 2007). Various spectral normalization techniques don't appear to affect the phase of the noise cross-correlations (Prieto *et al.*, 2011). Many studies have shown that the three components of the sensors, usually in the east (E)–north (N)–vertical (Z) reference frame can be rotated to T-R-Z reference frame after cross-correlation if the same temporal and spectral normalization factors are used for all components (Lin *et al.*, 2014; Nayak *et al.*, 2018). We will consider a three-component sensor at the source location with the components orientated in the T-R-Z reference frame and a single-component sensor at the receiver location with the component at an arbitrary direction X in the horizontal plane.

$$\langle v_i^*(\boldsymbol{x}_A, \omega) v_X(\boldsymbol{x}_B, \omega)\rangle \propto -G_{iX}(\boldsymbol{x}_A, \boldsymbol{x}_B, \omega) \quad \text{with } \; i = T, R, Z \tag{18}$$

Taking a spatial derivative in the X direction direction at the virtual receiver B,

$$\langle v_i^*(\boldsymbol{x}_A, \omega) \frac{\partial v_X(\boldsymbol{x}_B, \omega)}{\partial x_X}\rangle \propto -\frac{G_{iX}(\boldsymbol{x}_A, \boldsymbol{x}_B, \omega)}{\partial x_X} \tag{19}$$

The ensemble-averaged cross-correlation of noise in velocity at one sensor (virtual source) and noise in axial strain rate at the other sensor (virtual receiver) should converge to empirical axial strain in the same direction at the virtual receiver in response to single step forces at the virtual source. In this study, we focus on axial strain-rate noise records from DAS arrays. A single component measurement and arbitrary orientation of fiber-optic cables in DAS arrays, especially in pre-existing dark fiber, precludes any separation of the recorded surface-wave wavefield into Rayleigh waves or Love waves for simplified analysis. However, a three-component sensor as a virtual source in noise cross-correlations allows us to rotate the source components to a T-R-Z reference frame and analyze Rayleigh waves and Love waves recorded on DAS arrays separately.

Consider single forces applied at a source location in radial or tangential direction with respect to a particular channel of a DAS array oriented at angles $0^\circ \leq \theta \leq 90^\circ$ with respect to the wave propagation direction (Figure 3). The medium is 1D and isotropic. A radial force and tangential force will result in Rayleigh waves and Love waves with the maximum displacement in radial and tangential direction, respectively, and zero displacements in the orthogonal direction (Figure 3a-b, e-f). The displacement along the fiber at angles $0^\circ < \theta < 90^\circ$ is a vector sum of displacements in radial and tangential direction and still corresponds to pure Rayleigh waves and pure Love waves for the radial and tangential force, respectively, because displacement along one of the orthogonal directions is identically zero (Figure 3c, g). Therefore, for an ideal 1D and isotropic medium, displacements and strains at angles $0^\circ < \theta < 90^\circ$ correspond to pure Rayleigh waves and pure Love waves, for radial/vertical and tangential forces, respectively.

If a medium is weakly anisotropic or 3D, a radial force will generate small displacements in the tangential direction (RT) in addition to Rayleigh waves in the radial direction (RR) (Figure 3d). The net displacement along the X direction is given by $u_{RX} = u_{RR} \cos\theta + u_{RT} \sin\theta$; the direction cosine corresponding to the RR component is greater for $\theta \leq 45^\circ$. Rayleigh-wave strain amplitude varies as $\cos^2\theta$. Therefore, for small values of θ ($\lesssim 30^\circ$), the net displacement and strain along the fiber are expected to be dominated by Rayleigh waves. Similarly, a tangential force will generate small displacements in the radial direction (TR) in addition to Love waves in the tangential direction (TT) (Figure 3h). The direction cosine corresponding to the TT component displacement in the expression for net displacement along the X direction (u_{TX}) is greater for $\theta \geq 45°$. Love-wave strain amplitude varies as $\sin 2\theta$ with the maximum at $\theta = 45°$. Therefore, for $45° \lesssim \theta \lesssim 75°$, the net displacement and strain along the fiber are expected to be dominated by Love waves. We speculate that for a weakly 3D medium, a tangential force at the source is expected to generate Love-wave strains, and radial and vertical forces are expected to generate Rayleigh-wave strains for a range of favorable orientations. In the absence of a 3D velocity model, straight raypaths can be initially assumed for rotating the horizontal components of the seismometer acting as the virtual source to separate the Rayleigh and Love wavefields in the noise cross-correlations. Thereafter, the measured surface-wave phase traveltimes can be inverted for 3D velocity anomalies. For a smoothly varying initial or background 3D velocity model, it is possible to trace the minimum-time surface-wave raypaths for period-specific 2D phase velocity maps. The improved estimates of take-off azimuths at the source and arrival angles at the DAS array can be used to rotate the horizontal components of the seismometer and to calculate the phase correction factors (equations 7 and 12), respectively (Snieder, 1986; Yoshizawa and Kennett, 2004). The improved phase traveltime measurements can be used for iteratively updating the velocity model. In case of significant 3D structure or anisotropy, the displacement amplitudes on the RT and TR components can be comparable to those on the RR and TT components (Nayak *et al.*, 2018). In such conditions, the assumption that the strain response to radial/vertical and tangential forces corresponds to Rayleigh waves and Love waves, respectively, is likely to break down.

Hereinafter, we term the components of noise cross-correlations involving an inertial seismometer as a virtual source and channels of a DAS array as virtual receivers as TX, RX and ZX in which the first letter is the direction of the seismometer component or the single force applied at the source location and X is the arbitrary direction along which axial strain-rate noise or the empirical axial strain response is measured at the receiver location, which is the direction of the cable at a channel. T, R, and X directions are specific to each channel of the DAS array. In order to demonstrate the recovery of Love waves on the TX component and recovery of Rayleigh waves on the RX and ZX components of noise cross-correlations in a 1D isotropic medium, we perform synthetic tests on cross-correlation of synthetic ”noise” similar to Nayak *et al.* (2018) modified after (Herrmann, R.B., Update to do_mft for the determination of phase velocities from empirical Green's functions from noise cross-correlation, `www.eas.slu.edu/eqc/eqc_cps/TUTORIAL/EMPIRICAL_GREEN/index.html`, last accessed November 2020). In a 100 km × 100 km domain centered at the origin, three-component seismometers are placed in concentric circles of radii 12 km and 28 km, and at angular spacing $15°$ (Figure 4a). A hypothetical DAS array with channel spacing 0.2 km is laid along the x axis from -7 to +7 km (Figure 4a,b). For constructing synthetic noise records at the seismometers, we sum filtered (0.1–1.0 Hz) three-component velocity waveforms that are generated by randomly oriented force vectors (amplitude range –1 to +1) at random locations (but at least 50 m away from all receivers) on the surface with 20 sources acting simultaneously every three seconds (Figure 4a). The synthetics are fundamental mode surface-wave responses for the GIL7 model calculated using the modal summation method. We also calculate the net velocity response for the noise sources along the $+x$ direction at five receivers placed at 2 m spacing along the x axis centered at each channel of the DAS array (Figure 4c). For each channel (central receiver), the synthetic axial strain-rate noise along the $+x$ axis is calculated by numerical differentiation applied on velocity at the four neighboring receivers (equation 15). The exact methodology for noise cross-correlation applied to real data as described in the Appendix A1 is applied to 13 days of synthetic noise. For each source and channel, we rotate the final “noise” cross-correlations to TX, RX and ZX components. The cross-correlations of synthetic noise for a few “source” seismometers with the DAS array are compared with the theoretical axial strain response waveforms in response to input single step forces, $\frac{G_{iX}(\boldsymbol{x}_A,\boldsymbol{x}_B,\omega)}{\partial x_X}$ (equation 19) in Figure 5 and Figure S2.

As expected from conceptual arguments (Figure 3a-c,e-g), TX and (RX, ZX) component noise cross-correlation waveforms correspond to Love waves and Rayleigh waves, respectively, in idealized conditions (1D isotropic media and homogeneous distribution of background noise sources).

The cross-correlation waveforms show good comparison with theoretical responses. As expected, Love wave amplitudes are identically zero at $\theta = 0°, 90°, 180°$ and change polarity at $\theta = 90°$. Rayleigh wave amplitudes decrease towards zero at $\theta = 90°$. We recover meaningful Love waves for a wider range of angles ($\theta \sim 10° - 80°$) in the cross-correlations compared to Rayleigh waves ($\theta \sim 0° - 60°$) likely because Rayleigh wave amplitudes decay faster than Love wave amplitudes as a function of θ ($\cos^2\theta$ vs $\sin 2\theta$ variation).

We also measured surface-wave phase velocity dispersion on waveforms retrieved from cross-correlation of synthetic noise for seismometer sources in the outer circle (Figure 4a) using AFTAN analysis, incorporating the general phase correction factors derived in the previous section. In order to examine the errors as a function of θ, we do not apply any signal-to-noise ratio (SNR) threshold to select better measurements (Lin *et al.*, 2014) beyond the default quality control in the AFTAN method (Bensen *et al.*, 2007); this is justified because we did not add any random noise to the waveforms. In the following, the angle θ is defined to be the acute angle between surface-wave path and the direction of the axial strain (x axis) for simplicity. As shown in Figure 6 and Figure S3, the measured phase velocity dispersion is consistent with the predicted dispersion for the GIL7 model for a range of orientations for Rayleigh waves ($\theta \sim 0° - 45°$) and Love waves ($\theta \sim 15° - 75°$). The results for other angles show greater errors, which is primarily an effect of reduced amplitudes of Rayleigh waves and Love waves closer to $\theta \sim 90°$ and $\theta \sim 0°, 90°$, respectively. These results could doubtlessly be improved by expanding the domain over which the background noise sources are distributed (Figure 4a) and stacking noise cross-correlations for a longer period of time. The derived phase correction factors are valid for the entire range of θ. The temporal and spectral normalization methods applied on the strain-rate waveforms do not seem to cause any additional errors. For real data, we expect the analysis to be only limited by non-uniformity of background noise source distribution similar to the limitation for standard noise cross-correlation tomography applied to seismometer data only, and the presence of severe 3D structure or anisotropy that precludes the assumption that TX and (RX, ZX) component waveforms correspond to Love waves and Rayleigh waves, respectively.

Validation on Real Data

DAS array data were acquired on a dark fiber as part of the Lawrence Berkeley National Laboratory Fiber-Optic Sacramento Seismic Array experiment in the Sacramento basin, Northern California in 2017-2018 (Figure 7). The array consists of 23 km of dark fiber oriented primarily in two directions. Starting from the interrogator unit in West Sacramento, the recording profile first extends from an urban area into farmland near the Sacramento river in a northwest direction. It crosses Interstate 5 highway and then turns west towards the city of Woodland. The DAS data were acquired at 500 Hz, channel spacing of 2 m and gauge length of 10 m. The experiment also included a single broadband seismometer at the temporary station BB00 (Guralp CMG-3T, ∼120 s corner period) installed inside the Elkhorn Fire Station, 66 m northeast of channel 4800 and operated mostly in 2018. Further details about the DAS array, the broadband station, and the data acquisition are provided in Ajo-Franklin *et al.* (2019) and Lindsey *et al.* (2020).

We first calculate noise cross-correlations using data recorded by the DAS array for every 20^{th} channel (∼4 gauge lengths ∼40 m) and nearby permanent seismic stations, which include broadband sensors, vertical and three-component short-period sensors and accelerometers. The methodology for pre-processing the data and cross-correlation is described in Appendix A1. For each station and channel, we rotate the final noise cross-correlations to TX, RX and ZX components. Figure 8 shows the noise cross-correlations involving seismic stations and the DAS array. Similar to the DAS array, we calculated noise cross-correlations between the temporary broadband sensor and the regional permanent stations. These cross-correlations were rotated from the E-N-Z reference frame to the T-R-Z reference frame in the standard way (Lin *et al.*, 2014). For the same seismometer as the virtual source, we compare TX, RX and ZX components of cross-correlations involving the DAS array with the TT, RR, and ZR components of cross-correlations involving the temporary broadband station, respectively in Figure 8 (same force direction at the source, horizontal component at the receiver). The waveforms are filtered in the passband ∼0.1-0.4 Hz. Coherent seismic wave propagation with a well-defined moveout can be observed in the noise cross-correlations up to distances of ~80 km in the secondary microseism passband. Among the DAS array channels we utilize, channel 4791 is closest to the temporary broadband seismometer. The waveforms of the seismometer-DAS noise cross-correlations compare well with waveforms of seismometer-seismometer noise cross-correlations in terms of timing of the dominant phases and the relative amplitudes of the causal and anti-causal sides. We interpret the coherent waves in the TT and TX component waveforms as Love waves (Figure 8a,e), and waves in the RR, RX, ZR and ZX components as Rayleigh waves (Figure 8b,c,d,f). Other examples are shown in Figure S4. For stations present close to one end of the DAS array (SAC, Figure S4a), the Love waves moveout can be traced back to time t~0 s. For some virtual sources, the obvious change in the structure of waveforms at channels ~6700-7000 (e.g. Figure S4a) is due to the change in orientation of the DAS array from the southeast-northwest to the east-west direction. For paths to the DAS array that are approximately in the north-south direction, subparallel to the coast, the effect of inhomogeneous noise source distribution is evident in phases with moveout inconsistent with time t=0 at the source position (station OST, Figure S4f) (Stehly *et al.*, 2006; Stehly *et al.*, 2008; Ma *et al.*, 2013). In fact, the intrinsic array nature of DAS makes it suitable for locating anomalous background noise sources (Ma *et al.*, 2013). As expected from theory, almost no coherent waves are recovered at channels in the east-west segment (~7000-11000) for normal ($\theta \sim 90°$) surface-wave paths in either ZX or TX component (Figure S4d-f).

Dispersion is a characteristic of surface waves in multilayered media (Dziewonski *et al.*, 1969; Herrmann, 1973). In order to further verify the nature of waves observed in noise cross-correlations between the permanent seismometers and the DAS array, we compare the phase velocity dispersion measured on the cross-correlation waveforms for the channel closest to the temporary broadband station (channel 4791) with the phase velocity dispersion measured on cross-correlations with the temporary broadband station for the same virtual source seismometers. For the seismometer-DAS cross-correlations, we use AFTAN analysis with the general phase-correction factors (equations 7 and 12). Measurement of phase velocity dispersion for seismometer-seismometer cross-correlations was performed using standard AFTAN analysis. We used dispersion curves for a

1D model from a different section of the Great Valley (model CV0) (Nayak and Thurber, 2020) as reference. The methodology for calculating SNR for selecting good quality measurements is described in Appendix A2 in Nayak and Thurber (2020).

Figure 9 shows comparisons of group velocity and phase velocity dispersion measurements. We recovered coherent and well-isolated waves with good SNR on TX component waveforms for many source seismometers. There is an excellent match between Love-wave dispersion measured on the TX and TT components for many stations over a wide range of θ (Figure 9a). Unsurprisingly, cross-correlations with the temporary broadband seismometer yield more long period measurements. The measurement of Rayleigh-wave dispersion required more careful analysis. The study area is a deep sedimentary basin with the basin depth generally increasing towards west (Wentworth *et al*., 1995; Fletcher and Erdem, 2017). Sedimentary basins are known to generate strong-amplitude higher mode Rayleigh waves, especially in the radial component at the receiver (Ma *et al*., 2016). RX and ZX component waveforms showed complex long-duration arrivals that we inferred were possibly a combination of multiple Rayleigh waves modes. One of the benefits of multi-component noise cross-correlation involving two three-component seismometers is that fundamental and 1st higher mode Rayleigh waves can be clearly distinguished by their particle motion (retrograde vs prograde) on the [R/Z] components (Ma *et al*., 2016; Nayak and Thurber, 2020). However, the array nature of DAS can also be used to delineate velocities of different modes (Dou *et al*., 2017). In this study, we follow a simple approach for the comparisons. First, we identified virtual source stations that generated strong and clear 1st higher mode Rayleigh waves at the temporary broadband seismometer, identified using particle motion in the noise cross-correlations. Following the procedure in Nayak and Thurber (2020), we estimate an average time-series assuming prograde elliptical particle motion for measuring the dispersion curve. We selected the 1st higher mode (or 1st overtone) for comparison because it is expected to have greater amplitudes on noise cross-correlations for the DAS array, which correspond to the horizontal axial strain response of the medium. Many of these virtual source stations also generated waves with good SNR in similar time windows in the RX and ZX components of the seismometer-DAS noise cross-correlations.

For virtual source stations with a three-component sensor, we corrected the RX and ZX components for the phase difference in the two force directions at the source similar to Nayak and Thurber (2020) and averaged the two components to measure the dispersion curve. We also reduced the values of model CV0 reference dispersion curve by $\sim$5% for cross-correlations with station BDM to get realistic phase velocities in the measurements. We obtain a reasonably good match in the group and phase velocities for the 1st higher mode Rayleigh wave (Figure 9b). Paths to some stations such as BDM and 68034 traverse significant 3D structures, with seismic velocities increasing along these paths from the low-velocity sedimentary basin to the faster rocks of the Coast Ranges to the west (Fletcher and Erdem, 2017). Even for these paths, we observe fair agreement between phase velocities measured on seismometer-DAS and seismometer-seismometer noise cross-correlations (Figure 9), demonstrating reasonably good separation of Rayleigh and Love wavefields on the multi-component seismometer-DAS cross-correlations.

Conclusions

In this study, we derive expressions for phase of surface wave axial strain in an arbitrary direction, valid at far-field distances ($r \gtrsim \lambda$). This allows measurement of surface-wave phase velocity at single channels of DAS arrays and strainmeters in response to virtual sources or active sources such as vibroseis at local distances (i.e., at smaller distances than is possible assuming a plane wave) at any backazimuth. We develop the concept of retrieving empirical surface waves from mixed-sensor cross-correlation of velocity noise recorded by three-component seismometers and strain-rate noise recorded by DAS arrays. Using tests on cross-correlation of synthetic noise, we demonstrate that these cross-correlations converge to empirical axial strain response at the virtual receiver to single step forces applied at the virtual source and surface-wave phase velocity can be successfully measured using the expressions derived in this study. The combination of inertial seismometers and DAS arrays for passive imaging using ambient seismic noise offers significant advantages over the possibilities from noise cross-correlations using DAS arrays only,

(1) Using temporary (Parker *et al.*, 2018) or permanent seismometers distributed around DAS arrays, it is possible to extend surface-wave imaging using DAS arrays to 3D volumes, which has been mostly limited to 2D planes along straight segments of DAS arrays (Dou *et al.*, 2017; Zeng *et al.*, 2017; Ajo-Franklin *et al.*, 2019).

(2) It is possible to rotate the force directions of the three-component seismometer acting as a virtual source to the T-R-Z reference frame. We demonstrate the recovery of Love-wave strains on noise cross-correlations for tangential source direction both for synthetic noise and real data. This opens up the possibility of Love-wave tomography using a combination of three-component seismometers and DAS arrays. Recovery of Love waves using noise cross-correlation on DAS arrays only is difficult (Martin *et al.*, 2018) and passive surface-wave imaging using DAS arrays has been mostly limited to Rayleigh waves (Dou *et al.*, 2017; Zeng *et al.*, 2017; Ajo-Franklin *et al.*, 2019).

(3) In general, inertial seismometers have lower self-noise compared to individual channels of DAS arrays (Lellouch *et al.*, 2020). Therefore, noise cross-correlations combining the two types of sensors should allow us to recover useful surface waves at greater distances and longer periods than is possible using DAS-DAS noise cross-correlations. In this study, we demonstrate recovery of surface waves with good SNR at distances up to $\sim$80 km in the secondary microseism passband ($\sim$0.1-0.2 Hz) opening the possibility of high-resolution local and regional surface-wave tomography for crustal structure using data from DAS arrays.

In our study region, most seismic stations are at considerable distance from the DAS array ($\gtrsim$35 km) leading to the recovery of primarily longer period surface waves from noise cross-correlations, with maximum wavelengths longer than half of the total length of the DAS array. However, the theory and concepts developed in this study are expected to be valid at shorter distances and higher frequencies as well. Dark fiber resources for DAS are available in many regions with dense permanent seismic networks (Martin *et al.*, 2017; Martin and Biondi, 2018; Wang *et al.*, 2020). Dense temporary seismic networks may also be deployed along with DAS arrays (Zeng *et al.*, 2017; Parker *et al.*, 2018). The methods developed in this study can be applied to denser seismic networks surrounding a DAS array for traditional surface-wave tomography at shorter distances, higher frequencies and high spatial resolution. For longer period surface waves recovered using seismic stations at greater distances from the DAS array as in this study, we can use the difference of phase traveltimes at nearby channels instead of using the absolute phase traveltimes (Jin and Gaherty, 2015). The differential traveltimes can be precisely measured using cross-correlation methods and provide enhanced sensitivity to the velocity structure close to the DAS array.

Finally, we recommend that in noise cross-correlation studies involving seismometers and DAS arrays, it is beneficial to have a few three-component sensors close to the DAS arrays. Non-zero amplitudes on the TR, TZ, ZR, ZT components of the nine-component cross-correlation tensors involving seismometers only indicates the presence of severe 3D structure or anisotropy that will preclude the assumption that RX/ZX and TX components of seismometer-DAS noise cross-correlations correspond to Rayleigh waves and Love waves, respectively. Particle motion on multi-component noise cross-correlations are also helpful in identifying higher mode Rayleigh waves, if present.

Data and Resources

The permanent seismometer data used in this study primarily came from the following networks: Berkeley Digital Seismic Network (BK, doi:10.7932/BDSN) operated by the UC Berkeley Seismological Laboratory, the Northern California Seismic Network (NC, doi:10.7914/SN/NC) operated by the United States Geological Survey (USGS), California Division of Water Resources seismic network (WR), United States National Strong-Motion Network (NP) and California Strong Motion Instrumentation Program seismic network (CE). The data were downloaded through Northern California Earthquake Data Center (10.7932/NCEDC; `http://www.ncedc.org`, last accessed April 2018). Due to the very large size of the raw DAS dataset (~930 GB/day), only decimated data for limited intervals are available upon request. Codes for computing synthetic

Green's functions for 1-D velocity models by the modal summation method are available in the software Computer Programs in Seismology available at `http://www.eas.slu.edu/eqc/eqccps.html`, last accessed June 2020. ObsPy (Beyreuther *et al.*, 2010) and Seismic Analysis Code (Goldstein *et al.*, 2003) were used for downloading the data and basic analysis of seismograms. The maps were prepared using Generic Mapping Tools (Wessel *et al.*, 2013) and Google Earth.

The supplemental material includes detailed derivation of expressions for the phase of surface-wave axial strain in an arbitrary direction, and figures showing percentage error in the measured surface-wave phase velocity as a function of distance (r/λ) and θ for plane-wave approximation, more waveform comparisons between theoretical axial strain response to input single step forces and cross-correlations of synthetic velocity and strain-rate noise, more examples of phase velocity dispersion curves measured on cross-correlations of synthetic noise, and more examples of noise cross-correlations involving the Sacramento DAS array and nearby permanent seismic stations.

Acknowledgments

We thank the Editor-in-Chief T.L. Pratt, Editor C.I. Trifu, and reviewers A. Lellouch and R.B. Herrmann for their constructive comments and suggestions that significantly improved this study. The Imperial Valley Dark Fiber Team includes Feng Cheng, Veronica Rodriguez Tribaldos, Patrick Dobson, Todd Wood, Michelle Robertson, Robert Mellors, Cody Rotermund, Bin Dong, Inder Monga, Alex Popescu, Yucheng Shang, Emily Maher, Christina Morency, Eric Matzel, Elisabet Metcalfe, Lindsay Morse, Dennise Templeton, and Kesheng Wu.

This work was funded by the Office of Energy Efficiency and Renewable Energy, Geothermal Technologies Office, US Department of Energy (DOE) under Award Number DE-AC02-05CH11231 with Lawrence Berkeley National Laboratory (LBNL). The distributed acoustic sensing (DAS) data were acquired using the support of the Laboratory Directed Research and Development Program of LBNL under US DOE Contract No. DE-AC02-05CH11231. The data acquisition used resources of the ESnet Dark Fiber Testbed, which is supported by the Office of Science of the US DOE under contract DE-AC02-05CH11231. We acknowledge Nate Lindsey (FiberSense), Shan Dou (Teck Resources) and Craig Ulrich (LBNL) for assistance in the original Sacramento Array field effort. We would also like to acknowledge Chris Tracy (LBNL) for assistance with the data acquisition on ESnet's Dark Fiber Testbed. We thank Horst Rademacher (Berkeley Seismological Laboratory), Silixa, CenturyLink and Guralp for their assistance in data acquisition and Chief Yuong at the Elkhorn Fire Department for providing access to the broadband seismometer site. AN thanks R. B. Herrmann (St Louis University) for helpful suggestions and discussions on surface wave concepts and the strain response of body waves.

References

Ajo-Franklin, J. B., S. Dou, N. J. Lindsey, I. Monga, C. Tracy, M. M. Robertson, V. R. Tribaldos, C. Ulrich, B. Freifeld, T. M. Daley, and X. Li (2019). Distributed acoustic sensing using dark fiber for near-surface characterization and broadband seismic event detection. *Sci. Rep. 9*(1328), 1–14, doi: 10.1038/s41598-018- 36675-8.

Aki, K. and P. G. Richards (2002). *Quantitative Seismology* (2nd ed.). San Francisco, Calif., USA: University Science Books.

Bensen, G. D., M. H. Ritzwoller, M. P. Barmin, A. Levshin, F.-C. Lin, M. P. Moschetti, N. M. Shapiro, and Y. Yang (2007). Processing seismic ambient noise data to obtain reliable broadband surface wave dispersion measurements. *Geophys. J. Int. 169*(3), 1239–1260, doi: 10.1111/j.1365-246X.2007.03374.x.

Beyreuther, M., R. Barsch, L. Krischer, Y. B. T. Megies, and J. Wassermann (2010). ObsPy: A Python toolbox for seismology. *Seismol. Res. Lett. 81*(3), 530–533, doi: 10.1785/gssrl.81.3.530.

Blum, J., H. Igel, and M. Zumberge (2010). Observations of Rayleigh-wave phase velocity and coseismic deformation using an optical fiber, inter- ferometric vertical strainmeter at the SAFOD borehole, California. *Bull. Seismol. Soc. Am. 100*(5A), 1879–1891, doi: 10.1785/0120090333.

Daley, T. M., B. M. Freifeld, J. B. Ajo-Franklin, S. Dou, R. Pevzner, V. Shulakova, S. Kashikar, D. E. Miller, J. Goetz, J. Henninges, and S. Lueth (2013). Field testing of fiber-optic distributed acoustic sensing (DAS) for subsurface seismic monitoring. *Lead. Edge 32*(6), 699–706, doi: 10.1190/tle32060699.1.

Daley, T. M., D. E. Miller, K. Dodds, P. Cook, and B. M. Freifeld (2016). Field testing of modular borehole monitoring with simultaneous distributed acoustic sensing and geophone vertical seismic profiles at Citronelle, Alabama. *Geophys. Prosp. 64*(5), 1318–1334, doi: 10.1111/1365-2478.12324.

Dou, S., N. Lindsey, A. M. Wagner, T. M. Daley, B. Freifeld, M. Robertson, J. Peterson, C. Ulrich, E. R. Martin, and J. B. Ajo-Franklin (2017). Distributed acoustic sensing for seismic monitoring of the near surface: A traffic-noise interferometry case study. *Sci. Rep. 7*(11620), 1–12, doi: 10.1038/s41598-017-11986-4.

Dziewonski, A. M., S. Bloch, and M. Landisman (1969). A technique for the analysis of transient seismic signals. *Bull. Seismol. Soc. Am. 59*(1), 427–444.

Ekström, G., J. Tromp, and E. W. F. Larson (1997). Measurements and global models of surface wave propagation. *J. Geophys. Res. 102*(B4), 8137–8157.

Fletcher, J. and J. Erdem (2017). Shear-wave velocity model from Rayleigh wave group velocities centered on the Sacramento/San Joaquin Delta. *Pure App. Geophys. 174*(10), 3825–3839, doi: 10.1007/s00024-017-1587-x.

Goldstein, P., D. Dodge, M. Firpo, and L. Minner (2003). *SAC2000: Signal processing and analysis tools for seismologists and engineers. Invited contribution to The IASPEI International Handbook of Earthquake and Engineering Seismology, W. H. K. Lee, H. Kanamori, P. C. Jennings, and C. Kisslinger (Editors)*. London: Academic Press.

Gomberg, J. and D. Agnew (1996). The accuracy of seismic estimates of dynamic strains: an evaluation using strainmeter and seismometer data from Pinon Flat Observatory. *Bull. Seismol. Soc. Am. 86*(1A), 212–220.

Gouedard, P., T. Seher, J. J. McGuire, J. A. Collins, and R. D. van der Hilst (2014). Correction of ocean-bottom seismometer instrumental clock errors using ambient seismic noise. *Bull. Seismol. Soc. Am. 104*(3), 1276–1288, doi: 10.1785/0120130157.

Hartog, A. (2017). *An introduction to distributed optical fiber sensors*. Boca Raton, FL, USA: CRC Press.

Herrmann, R. B. (1973). Some aspects of band-pass filtering of surface waves. *Bull. Seismol. Soc. Am. 63*(2), 663–671.

Herrmann, R. B. (2013). Computer programs in seismology: An evolving tool for instruction and research. *Seismol. Res. Lett. 84*(6), 1081–1088, doi: 10.1785/0220110096.

Herrmann, R. B. (2014). Notes on multiple filter theory. `http://www.eas.slu.edu/eqc/eqc_cps/TUTORIAL/EMPIRICAL_GREEN/MFT.pdf`, last accessed November 2020 .

Jin, G. and J. B. Gaherty (2015). Surface wave phase-velocity tomography based on multichannel cross-correlation. *Geophys. J. Int. 201*(3), 1383–1398, doi: 10.1093/gji/ggv079.

Jousset, P., T. Reinsch, T. Ryberg, H. Blanck, A. Clarke, R. Aghayev, G. Hersir, J. Henninges, M. Weber, and C. M. Krawczyk (2018). Dynamic strain determination using fibre-optic cables allows imaging of seismological and structural features. *Nat. Commun. 9*(2509), 1–11, doi: 10.1038/s41467-018-04860-y.

Karrenbach, M., Z. Shen, Z. Li, S. Cole, E. Williams, A. Klesh, X. Wang, Z. Zhan, L. LaFlame, V. Yartsev, and V. Bogdanov (2020). Rapid deployment of Distributed Acoustic Sensing systems to track earthquake activity. *SEG Expanded Abstracts*, 490–494, doi: 10.1190/segam2020-3426905.1.

Kuvshinov, B. N. (2016). Interaction of helically wound fibre-optic cables with plane seismic waves. *Geophys. Prosp. 64*(3), 671–688, doi: 10.1111/1365-2478.12303.

Lellouch, A., N. J. Lindsey, W. L. Ellsworth, and B. L. Biondi (2020). Comparison between Distributed Acoustic Sensing and geophones: Downhole microseismic monitoring of the FORGE Geothermal Experiment. *Seismol. Res. Lett. 91*(6), 3256–3268, doi: 10.1785/0220200149.

Lin, F.-C., D. Li, R. W. Clayton, and D. Hollis (2013). High-resolution 3D shallow crustal structure in Long Beach, California: Application of ambient noise tomography on a dense seismic array. *Geophysics 78*(4), Q45–Q56.

Lin, F.-C., M. P. Moschetti, and M. H. Ritzwoller (2008). Surface wave tomography of the western United States from ambient seismic noise: Rayleigh and Love wave phase velocity maps. *Geophys. J. Int. 173*, 281–298.

Lin, F.-C., V. C. Tsai, and B. Schmandt (2014). 3-D crustal structure of the western United States: application of Rayleigh-wave ellipticity extracted from noise cross-correlations. *Geophys. J. Int. 198*, 656–670.

Lindsey, N. J., E. R. Martin, D. S. Dreger, B. Freifeld, S. Cole, S. R. James, B. L. Biondi, and J. B. Ajo-Franklin (2017). Fiber-Optic Network Observations of Earthquake Wavefields. *Geophys. Res. Lett. 44*(23), 11792–11799, doi: 10.1002/2017GL075722.

Lindsey, N. J., H. Rademacher, and J. B. Ajo-Franklin (2020). On the broadband instrument response of fiber-optic DAS arrays. *J. Geophys. Res. Solid Earth 125*(2), 1–16, doi: 10.1029/2019JB018145.

Luo, B., W. Trainor-Guitton, E. Bozdag, L. LaFlame, S. Cole, and M. Karrenbach (2020). Horizontally orthogonal distributed acoustic sensing array for earthquake- and ambient-noise-based multichannel analysis of surface waves. *Geophys. J. Int. 222*(3), 2147–2161, doi: 10.1093/gji/ggaa293.

Ma, Y., R. W. Clayton, and D. Li (2016). Higher-mode ambient-noise Rayleigh waves in sedimentary basins. *Geophys. J. Int. 206*(3), 1634–1644, doi: 10.1093/gji/ggw235.

Ma, Y., R. W. Clayton, V. Tsai, and Z. Zhan (2013). Locating a scatterer in the active volcanic area of Southern Peru from ambient noise cross- correlation. *Geophys. J. Int. 192*(3), 1332–1341, doi: 10.1093/gji/ggs103.

Martin, E. R. and B. L. Biondi (2018). Eighteen months of continuous near-surface monitoring with DAS data collected under Stanford University. Paper presented at 88th SEG International Annual Meeting, Anaheim, CA, doi:10.1190/segam2018-2997853.1.

Martin, E. R., C. M. Castillo, S. Cole, P. S. Sawasdee, S. Yuan, R. Clapp, M. Karrenbach, and B. L. Biondi (2017). Seismic monitoring leveraging existing telecom infrastructure at the SDASA: Active, passive, and ambient-noise analysis. *Lead. Edge 36*(12), 1025–1031, doi: 10.1190/tle36121025.1.

Martin, E. R., N. Lindsey, J. Ajo-Franklin, and B. L. Biondi (2018). Introduction to interferometry of fiber optic strain measurements. EarthArXiv.

Mateeva, A., J. Lopez, H. Potters, J. Mestayer, B. Cox, D. Kiyashchenko, P. Wills, S. Grandi, K. Hornman, B. Kuvshinov, W. Berlang, Z. Yang, and R. Detomo (2014). Distributed acoustic sensing for reservoir monitoring with vertical seismic profiling. *Geophys. Prosp. 62*(4), 679–692, doi: 10.1111/1365-2478.12116.

Nayak, A., D. Eberhart-Phillips, N. A. Ruppert, H. Fang, M. M. Moore, C. Tape, D. H. Christensen, G. A. Abers, and C. H. Thurber (2020). 3D seismic velocity models for Alaska from joint tomographic inversion of body-wave and surface-wave data. *Seismol. Res. Lett. 91*(6), 3106–3119, doi: 10.1785/0220200214.

Nayak, A., T. Taira, D. S. Dreger, and R. Gritto (2018). Empirical Green's tensor retrieved from ambient noise cross-correlations at The Geysers geothermal field, Northern California. *Geophys. J. Int. 213*, 340–369, doi: 10.1093/gji/ggx534.

Nayak, A. and C. H. Thurber (2020). Using multi-component ambient seismic noise cross-correlations to identify higher mode Rayleigh waves and improve dispersion measurements. *Geophys. J. Int. 222*, 1590–1605, doi: 10.1093/gji/ggaa270.

Ning, I. L. C. and P. Sava (2018). Multicomponent distributed acoustic sensing: concept and theory. *Geophysics 83*(2), P1–P8, doi: 10.1190/GEO2017-0327.1.

Nishida, K., H. Kawakatsu, and K. Obara (2008). Three-dimensional crustal S wave velocity structure in Japan using microseismic data recorded by Hi-net tiltmeters. *J. Geophys. Res. 113*(B10302), 1–22, doi: 10.1029/2007JB005395.

Paitz, P., K. Sager, and A. Fichtner (2019). Rotation and strain ambient noise interferometry. *Geophys. J. Int. 216*(3), 1938–1952, doi: 10.1093/gji/ggy528.

Parker, L. M., C. H. Thurber, X. Zeng, P. Li, N. E. Lord, D. Fratta, H. F. Wang, M. C. Robertson, A. Thomas, M. Karplus, A. Nayak, and K. Feigl (2018). Active-source seismic tomography at the Brady geothermal field, Nevada, with dense nodal and fiber-optic seismic arrays. *Seismol. Res. Lett. 89*(5), 1629–1640, doi: 10.1785/0220180085.

Prieto, G. A., M. A. Denolle, J. F. Lawrence, and G. Beroza (2011). On amplitude information carried by the ambient seismic field. *C. R. Geosci. 343*(8-9), 600–614, doi: 10.1016/j.crte.2011.03.006.

Roux, P., L. Moreau, A. Lecointre, G. Hillers, M. Campillo, Y. Ben-Zion, D. Zigone, and F. Vernon (2016). A methodological approach towards high-resolution surface wave imaging of the San Jacinto Fault Zone using ambient-noise recordings at a spatially dense array. *Geophys. J. Int. 206*(2), 989–992, doi: 10.1093/gji/ggw193.

Shapiro, N. M. and M. Campillo (2004). Emergence of broadband Rayleigh waves from correlations of the ambient seismic noise. *Geophys. Res. Lett. 31*, doi: 10.1029/2004GL019491.

Shapiro, N. M., M. Campillo, L. Stehly, and M. H. Ritzwoller (2005). High-resolution surface-wave tomography from ambient seismic noise. *Science 307*, 1615–1618.

Snieder, R. (1986). 3-D linearized scattering of surface waves and a formalism for surface wave holography. *Geophys. J. R. Astron. Soc. 84*, 581–605.

Song, Z., X. Zeng, and C. H. Thurber (2021). Surface-wave dispersion spectrum inversion method applied to Love and Rayleigh waves recorded by distributed acoustic sensing. *Geophysics 86*(1), EN1–EN12, doi: 10.1190/GEO2019-0691.1.

Stehly, L., M. Campillo, B. Froment, and R. L. Weaver (2008). Reconstructing Green's function by correlation of the coda of the correlation (C3) of ambient seismic noise. *J. Geophys. Res. Solid Earth 113*(B11306), 1–10, doi: 10.1029/2008JB005693.

Stehly, L., M. Campillo, and N. M. Shapiro (2006). A study of the seismic noise from its long-range correlation properties. *J. Geophys. Res. 111*(B10306), 1–12, doi: 10.1029/2005JB004237.

Stidham, C., M. Antolik, D. Dreger, S. Larsen, and B. Romanowicz (1999). Three-dimensional structure influences on the strong motion wave- field of the 1989 Loma Prieta earthquake. *Bull. Seismol. Soc. Am. 89*(5), 118–1202.

Wang, H., X. Zeng, D. E. Miller, D. Fratta, C. H. T. K. L. Feigl, and R. J. Mellors (2018). Ground motion response to an ML 4.3 earthquake using co-located distributed acoustic sensing and seismometer arrays . *Geophys. J. Int. 213*(3), 2020–2036, doi: 10.1093/gji/ggy102.

Wang, X., E. F. Williams, M. Karrenbach, M. G. Herráez, H. F. Martins, and Z. Zhan (2020). Rose parade seismology: signatures of floats and bands on optical fiber. *Seismol. Res. Lett. 91*(4), 2395–2398, doi: 10.1785/0220200091.

Wentworth, C. M., G. R. Fisher, P. Levine, and R. C. Jachens (1995). The surface of crystalline basement, Great Valley and Sierra Nevada, California: A digital map database. U.S. Geological Survey Open-File Report 95-96 .

Wessel, P., W. Smith, R. Scharroo, J. Luis, and F. Wobbe (2013). Generic mapping tools: improved version released. *Eos Trans. Am. Geophys. Un. 94*(45), 409–410, doi: 10.1002/2013EO450001.

Yao, H., R. D. van der Hilst, and M. V. de Hoop (2006). Surface-wave array tomography in SE Tibet from ambient seismic noise and two-station analysis – I. Phase velocity maps. *Geophys. J. Int. 166*(2), 732–744, doi: 10.1111/j.1365-246X.2006.03028.x.

Yoshizawa, K. and B. L. N. Kennett (2004). Multimode surface wave tomography for the Australian region using a three-stage approach incorporating finite frequency effects. *J. Geophys. Res. 109*(B02310), 1–19, doi: 10.1029/2002JB002254.

Yu, C., Z. Zhan, N. J. Lindsey, J. B. A. Franklin, and M. Robertson (2019). The potential of DAS in teleseismic studies: Insights from the Goldstone experiment. *Geophys. Res. Lett. 46*(3), 1320–1328, doi: 10.1029/2018GL081195.

Zeng, X., C. Lancelle, C. H. Thurber, D. Fratta, H. Wang, N. Lord, A. Chalari, and A. Clarke (2017). Properties of noise cross-correlation functions Obtained from a Distributed Acoustic Sensing Array at Garner Valley. *Bull. Seismol. Soc. Am. 107*(2), 603–610, doi: 10.1785/0120160168.

Zeng, X., C. H. Thurber, H. Wang, D. Fratta, E. Matzel, and the PoroTomo Team (2017). High-resolution Shallow Structure Revealed with Ambient Noise Tomography on a Dense Array. Proceedings, 42nd Workshop on Geothermal Reservoir Engineering Stanford University, Stanford, California, February 13-15, 2017 SGP-TR-212.

Zhu, T., J. Shen, and E. R. Martin (2021). Sensing Earth and environment dynamics by telecommunication fiber-optic sensors: an urban experiment in Pennsylvania, USA. *Solid Earth 12*(1), 219–235, doi: 10.5194/se-12-219-2021.

Avinash Nayak
1 Cyclotron Road,
LBNL M/S 74R316C,
Berkeley, CA 94720, USA.
anayak7@lbl.gov

Jonathan Ajo-Franklin
6100 Main Street,
Dept. of Earth, Environmental, and Planetary Sciences,
Rice University, MS-126,
Houston, TX 77005, USA.
ja62@rice.edu

Figure Captions

Figure 1. (a) Geometry for the derivation of expressions for surface-wave axial strain. The black line with an arrow points to the direction of surface wave propagation, at an angle ψ with respect to $+x$ axis. Rayleigh wave (blue) and Love wave (green) particle displacements are indicated. The red line with an arrow points to the direction in which axial strain is to be measured, at an angle of φ with respect to $+x$ axis. $\theta = \psi - \varphi$. (b) Source-receiver geometry for calculating synthetic waveforms to validate the expressions for surface-wave axial strain. Black triangles are three-component sources. Red '+' marks are five receivers lying along the x axis at 2 m spacing, centered at the origin. (c) A view zooming in on the receivers.

Figure 2. (a) Rayleigh-wave phase velocity dispersion curves measured on synthetic axial strain waveforms incorporating the phase correction factor ϕ' in the AFTAN analysis. The dispersion curves are color-coded by the angle between wave propagation and direction of strain measurement (θ). Different columns are for three different distances, 30 km, 60 km and 90 km. The black curve is the predicted Rayleigh-wave dispersion curve for the GIL7 model. (b) Same as (a) but for plane-wave approximation. (c) Same as (a) but for Love-wave dispersion. (d) Same as (b) but for Love-wave dispersion. Rayleigh-wave dispersion at $\theta = 90°$ and and Love-wave dispersion at $\theta = 0°, 90°, 180°$ are not shown because the waveforms are identically zero.

Figure 3. The black arrow represents surface-wave raypath from the source, a three-component sensor (black triangle) to the receiver (black circle), a channel of a DAS array (red line) which is oriented at an angle θ with respect to the surface-wave path and measures axial strain in that direction. First and second column plots are for $\theta = 0°$ and $\theta = 90°$, respectively, and the 3rd and 4th column plots are for intermediate angles. Colored arrows at the source indicate single forces applied in the radial (blue, top row plots) or tangential (green, bottom row plots) direction. For 1D isotropic media (plots in the first three columns), colored arrows at the receivers indicate particle displacement - (Rayleigh wave, radial, blue) or (Love wave, tangential, green). The displacement

in the other orthogonal directions is zero. The plots in the 4th column are for a weakly 3D media in which a single force generates non-zero displacement in both orthogonal directions. In plots in the last two columns, the arrow in the direction of the DAS array represents the net displacement in that direction. It is pure Rayleigh wave and Love wave in (c) and (g), respectively, and is dominated by Rayleigh waves and Love waves in (d) and (h), respectively. The colored waveforms (c-d, g-h) represent a breakdown of the contribution of the waves in the radial (blue) and tangential (green) directions. In (f), while the Love-wave displacement is non-zero, the strain is zero.

Figure 4. (a) Source-receiver geometry for synthetic tests on cross-correlations of synthetic noise recorded by three-component inertial seismometers (black triangles) and a DAS array (red + signs). Gray stars are random noise sources generated on the surface in 1 min. Sources in the inner and outer circles are numbered 1, 2,. . . . and 1F, 2F,. . . ., respectively, in anti-clockwise direction from $-x$ axis. Noise cross-correlation waveforms for sources marked 1, 3 and 7 spanning the DAS array are shown in Figure 5. The corresponding waveforms for sources marked 2, 4 and 5 are shown in Figure S2. (b) View zooming in on the DAS array. (c) Similar to Figure 1c, view focusing on a single channel element with two receivers placed on each side at 2 m spacing for calculating axial strain-rate along the x axis using numerical differentiation.

Figure 5. Figures showing comparisons of theoretical axial strain response to input single step forces (red waveforms) and waveforms retrieved from noise cross-correlation (black) of synthetic velocity noise recorded at a three-component seismometer acting as a virtual source and synthetic axial strain-rate noise recorded by channels of a DAS array acting as virtual receivers (Figure 4). (a), (b), and (c) are for sources marked 1, 3, and 7, respectively. The waveforms are arranged by distance in (a) with $\theta = 0°$, and by θ in (b) and (c). The waveforms are filtered at 0.4-1.0 Hz using a zero-phase Butterworth filter. The three columns correspond to TX, RX and ZX components (indicated at the top left corner). Similar plots for sources 2, 4 and 5 are shown in Figure S2.

Figure 6. Phase velocity dispersion curves measured on the cross-correlations of synthetic noise

(e.g. black waveforms shown in Figure 5). Plots in (a) and (b) show Rayleigh-wave and Love-wave dispersion measured on the ZX and TX components, respectively. Different plots are for different virtual sources (seismometers in the outer circle, Figure 4a); the source and the average θ are indicated on the top left corner. In each plot, the dispersion curves are for cross-correlations for the same seismometer with all channels of the DAS array, color-coded by θ ($\lesssim \pm 10^{\circ}$ from the average value). The black curves are the predicted dispersion curves for the GIL7 model.

Figure 7. Map of the study area. (a) The solid black curve is the Lawrence Berkeley National Laboratory distributed acoustic sensing (DAS) array at Sacramento. Other symbols are permanent seismic stations (names indicated) – black triangle (broadband sensor), magenta diamond (three-component short-period sensor), blue triangle (vertical component short-period sensor), and red square (accelerometer). Some short-period sensors and accelerometers are installed in boreholes. The area marked by dashed white rectangle is expanded in panel (b). (b) In this Google Earth image, thick solid cyan line is the DAS array. Numbers in white indicate locations of specific channels for reference. Each 1000-channel cable segment is $\sim$2 km long. The location of the single broadband seismometer (BB00, red star), I-5 highway (dashed yellow line) and nearby cities are also marked.

Figure 8. Each plot shows noise cross-correlation waveforms involving a specific regional permanent seismic station acting as the virtual source. The network and station name are indicated near the top of the plots in blue (format network.station). The gray waveforms are cross-correlations with channels of the DAS array arranged by distance. The red waveforms are cross-correlations with the temporary broadband station. The color-coded components corresponding to the two types of cross-correlations are indicated in the top right corner of each plot. Channel numbers for some channels of the DAS array (in red) are indicated next to the waveforms for reference. The type of sensors at the permanent stations are – broadband (BDM), vertical-component short-period (NBP and NDH), and accelerometer (68034). See Figure 7a for station locations.

Figure 9. Comparison of surface-wave dispersion curves measured on seismometer-seismometer ("BB00", red) and seismometer-DAS ("DAS 4791", black) noise cross-correlations for the DAS channel (4791) closest to the temporary broadband seismometer. (a) Fundamental mode Love wave (b) 1st higher mode Rayleigh wave. Each plot is for a specific permanent seismic station acting as the virtual source – network and station name (format network.station), distance and the angle θ are indicated at the top of each plot. C: Phase velocity (+), U: Group Velocity (o). Dashed blue line is the reference dispersion curve. See Figure 7a for station locations.

Appendix A1 Noise cross-correlation methodology

The methodology used for pre-processing inertial seismometer data and calculating noise cross-correlations is similar to that of Nayak and Thurber (2020) (see Appendix A3 in Nayak and Thurber (2020)). Most importantly, we use the same temporal and spectral normalization factors for all three components of a seismometer in order to preserve the relative amplitudes between the components (Lin *et al*., 2014). We decimate the seismometer data downloaded in 1-day-long time series to 10 Hz after correcting for the instrument response to velocity. For the DAS strain-rate data, data segments of 1 min duration are appended to 1.5-hour durations, detrended and tapered, decimated to 10 Hz and then appended to 1-day long time-series. Following Lindsey *et al*. (2020), we assume a flat phase response for the DAS data in the frequency range of interest. The DAS data is treated as a single-component seismometer data for temporal and spectral normalization. The frequency passbands for calculating amplitude envelopes for temporal normalization are 0.05-0.15 Hz, 0.15-1.0 Hz and 0.05-1.0 Hz. During the spectral normalization step, the data is kept bandlimited in the passband 0.05-1.0 Hz. The DAS noise cross-correlations are between seismometer components in E, N and Z directions and DAS channels oriented in arbitrary directions (X). The noise cross-correlations involving seismometers only were done in the E-N-Z reference frame. The cross-correlations for all 30-minute windows (with 75% overlap) in one day are stacked to form a daily average and the averages are stacked for all available days to form a final reference stack. We average the causal and anticausal sides of the final stacked cross-correlations, extracting the symmetric component. During the data acquisition, both the DAS interrogator and the temporary broadband seismometer suffered from clock failure. The clock errors for the two instruments were corrected independently by estimating time shifts required to make the causal and anti-causal side of cross-correlations with permanent stations as symmetric as possible (Gouedard *et al*., 2014). For the cross-correlation of synthetic noise, the surface-wave velocity synthetics are originally calculated at 20 Hz and the final 1-day-long synthetic noise time-series is decimated to 10 Hz prior to noise cross-correlation.

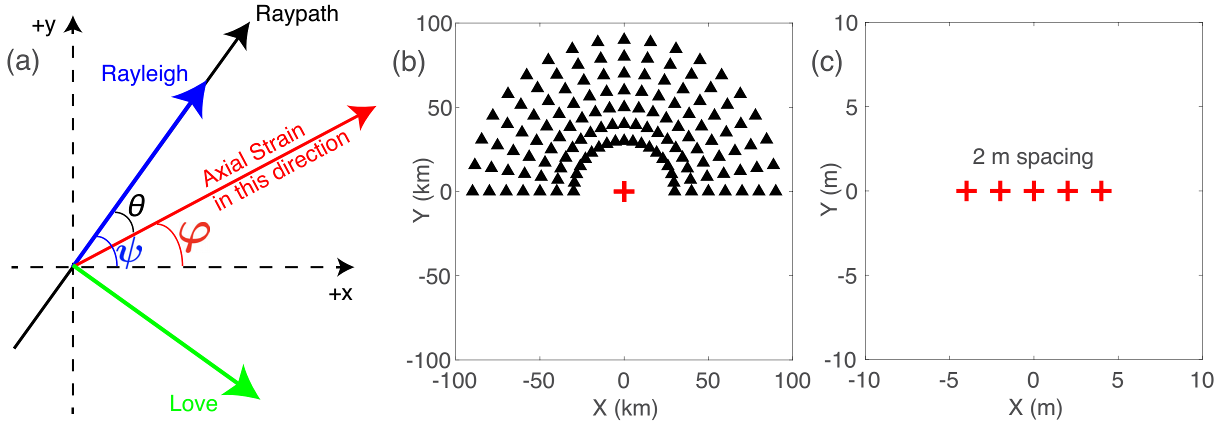

Figure 1. (a) Geometry for the derivation of expressions for surface-wave axial strain. The black line with an arrow points to the direction of surface wave propagation, at an angle ψ with respect to $+x$ axis. Rayleigh wave (blue) and Love wave (green) particle displacements are indicated. The red line with an arrow points to the direction in which axial strain is to be measured, at an angle of φ with respect to $+x$ axis. $\theta = \psi - \varphi$. (b) Source-receiver geometry for calculating synthetic waveforms to validate the expressions for surface-wave axial strain. Black triangles are three-component sources. Red '+' marks are five receivers lying along the x axis at 2 m spacing, centered at the origin. (c) A view zooming in on the receivers.

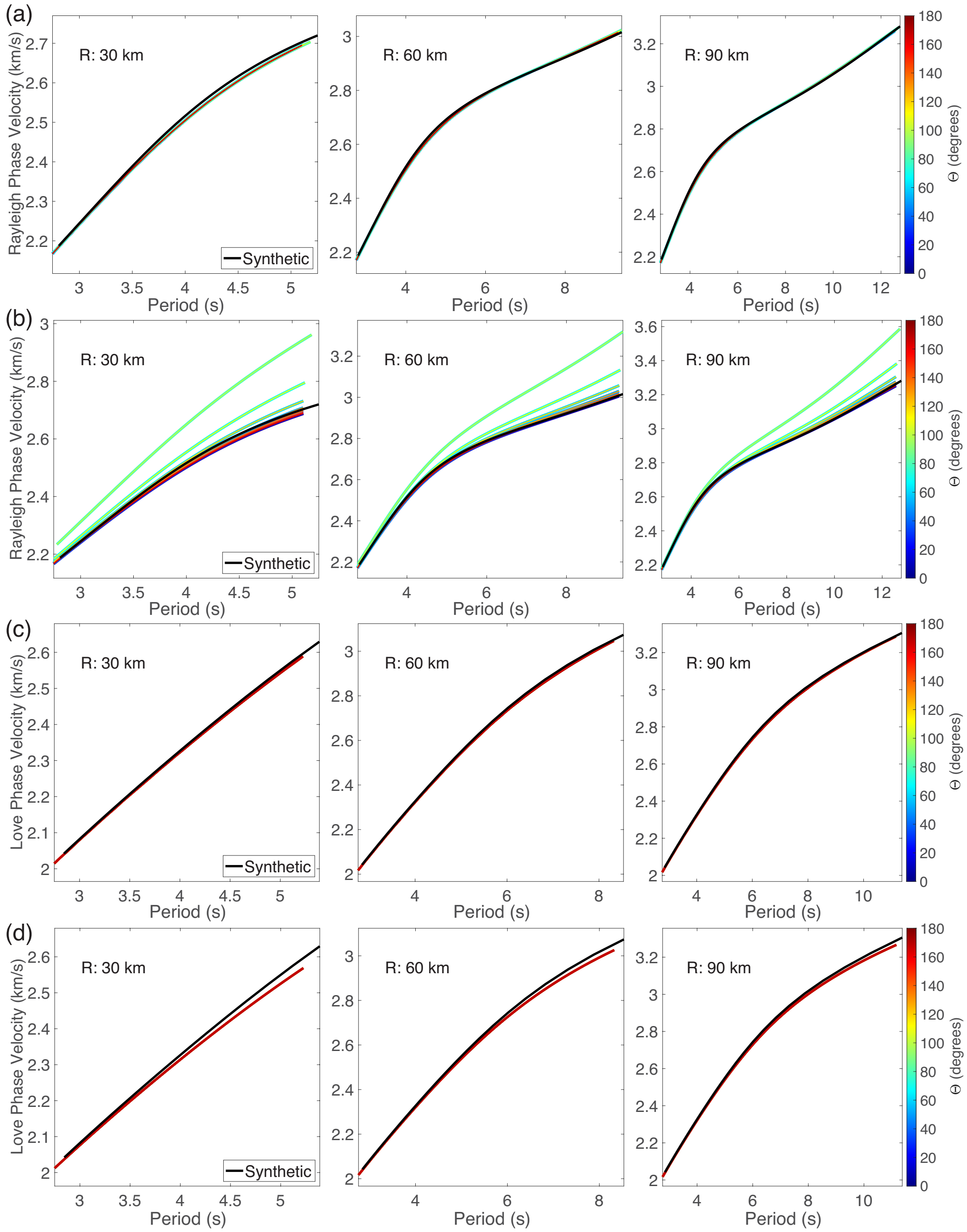

Figure 2. (a) Rayleigh-wave phase velocity dispersion curves measured on synthetic axial strain waveforms incorporating the phase correction factor ϕ' in the AFTAN analysis. The dispersion curves are color-coded by the angle between wave propagation and direction of strain measurement (θ). Different columns are for three different distances, 30 km, 60 km and 90 km. The black curve is the predicted Rayleigh-wave dispersion curve for the GIL7 model. (b) Same as (a) but for plane-wave approximation. (c) Same as (a) but for Love-wave dispersion. (d) Same as (b) but for Love-wave dispersion. Rayleigh-wave dispersion at $\theta = 90°$ and and Love-wave dispersion at $\theta = 0°, 90°, 180°$ are not shown because the waveforms are identically zero.

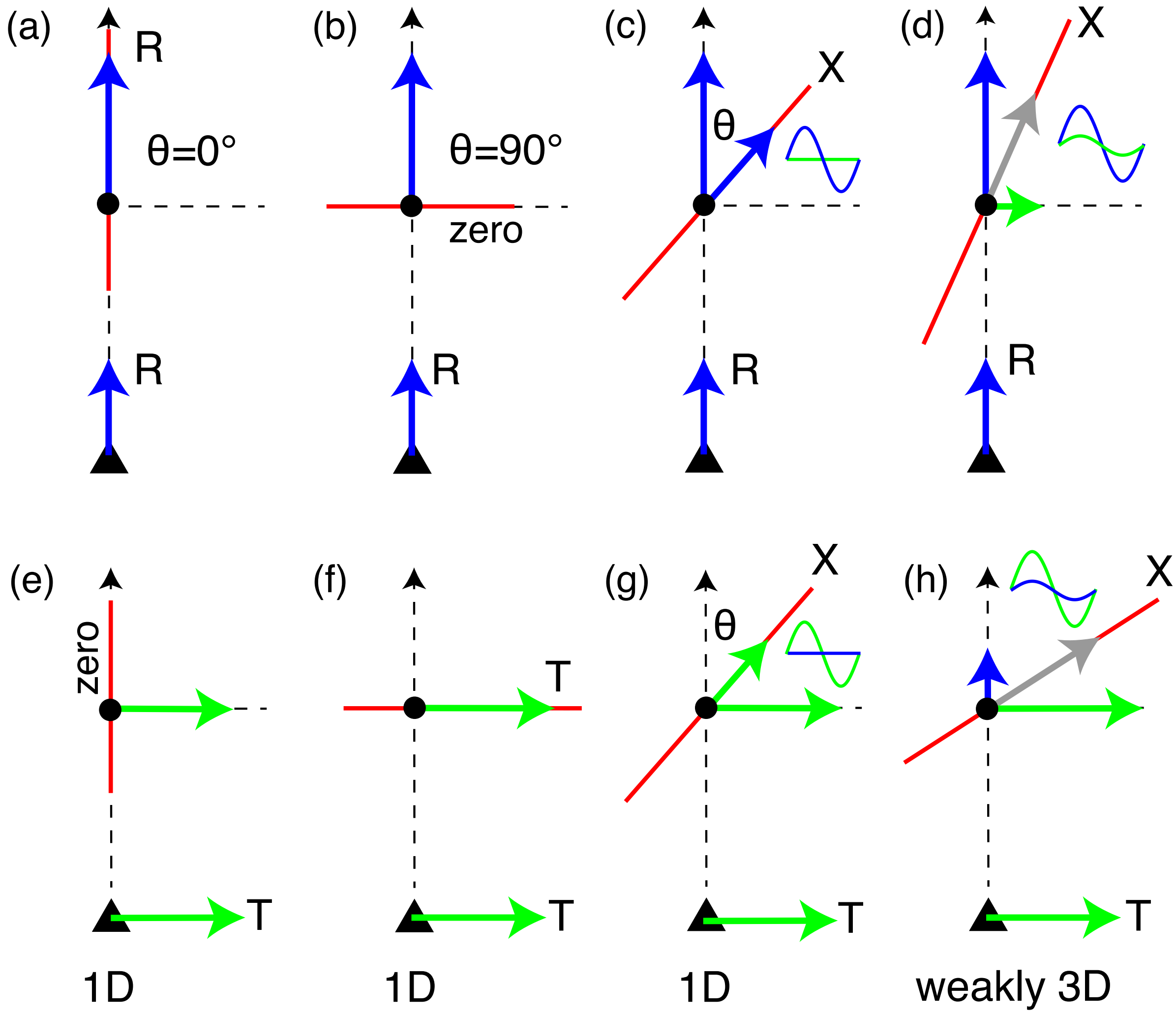

Figure 3. The black arrow represents surface-wave raypath from the source, a three-component sensor (black triangle) to the receiver (black circle), a channel of a DAS array (red line) which is oriented at an angle θ with respect to the surface-wave path and measures axial strain in that direction. First and second column plots are for $\theta = 0°$ and $\theta = 90°$, respectively, and the 3rd and 4th column plots are for intermediate angles. Colored arrows at the source indicate single forces applied in the radial (blue, top row plots) or tangential (green, bottom row plots) direction. For 1D isotropic media (plots in the first three columns), colored arrows at the receivers indicate particle displacement - (Rayleigh wave, radial, blue) or (Love wave, tangential, green). The displacement in the other orthogonal directions is zero. The plots in the 4th column are for a weakly 3D media in which a single force generates non-zero displacement in both orthogonal directions. In plots in the last two columns, the arrow in the direction of the DAS array represents the net displacement in that direction. It is pure Rayleigh wave and Love wave in (c) and (g), respectively, and is dominated by Rayleigh waves and Love waves in (d) and (h), respectively. The colored waveforms (c-d, g-h) represent a breakdown of the contribution of the waves in the radial (blue) and tangential (green) directions. In (f), while the Love-wave displacement is non-zero, the strain is zero.

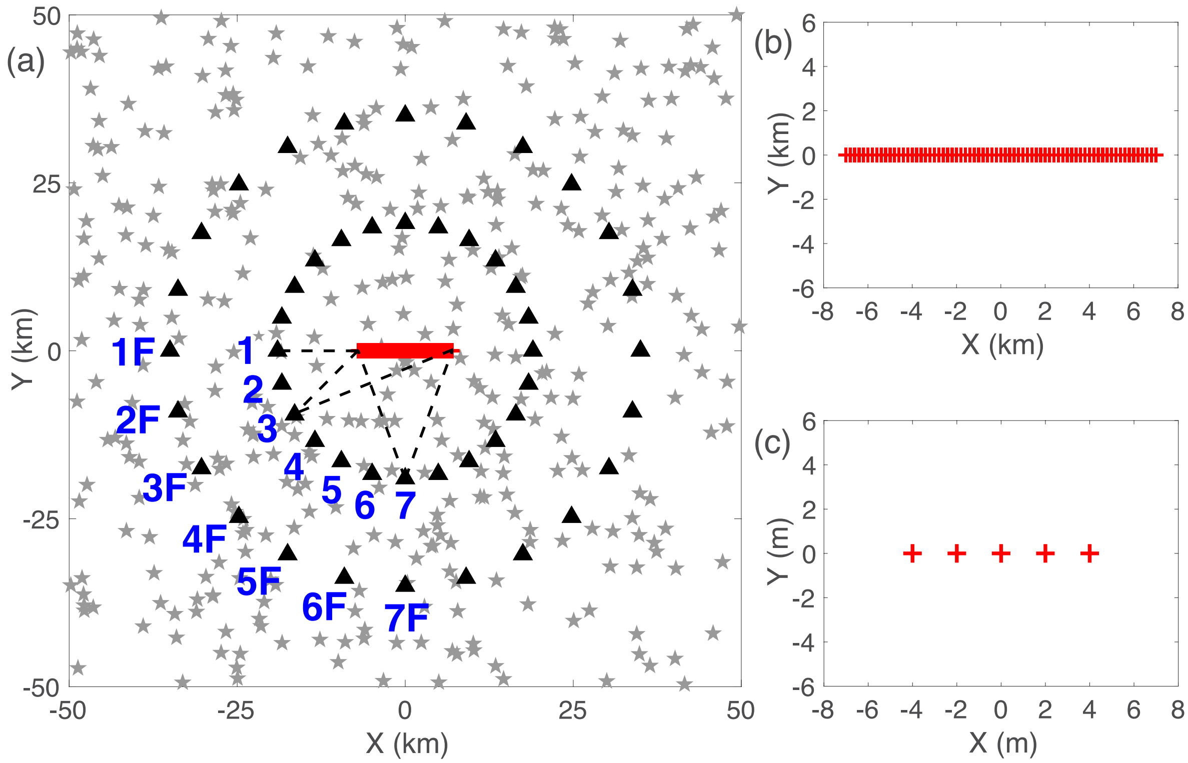

Figure 4. (a) Source-receiver geometry for synthetic tests on cross-correlations of synthetic noise recorded by three-component inertial seismometers (black triangles) and a DAS array (red + signs). Gray stars are random noise sources generated on the surface in 1 min. Sources in the inner and outer circles are numbered 1, 2,.... and 1F, 2F,...., respectively, in anti-clockwise direction from $-x$ axis. Noise cross-correlation waveforms for sources marked 1, 3 and 7 spanning the DAS array are shown in Figure 5. The corresponding waveforms for sources marked 2, 4 and 5 are shown in Figure S2. (b) View zooming in on the DAS array. (c) Similar to Figure 1c, view focusing on a single channel element with two receivers placed on each side at 2 m spacing for calculating axial strain-rate along the x axis using numerical differentiation.

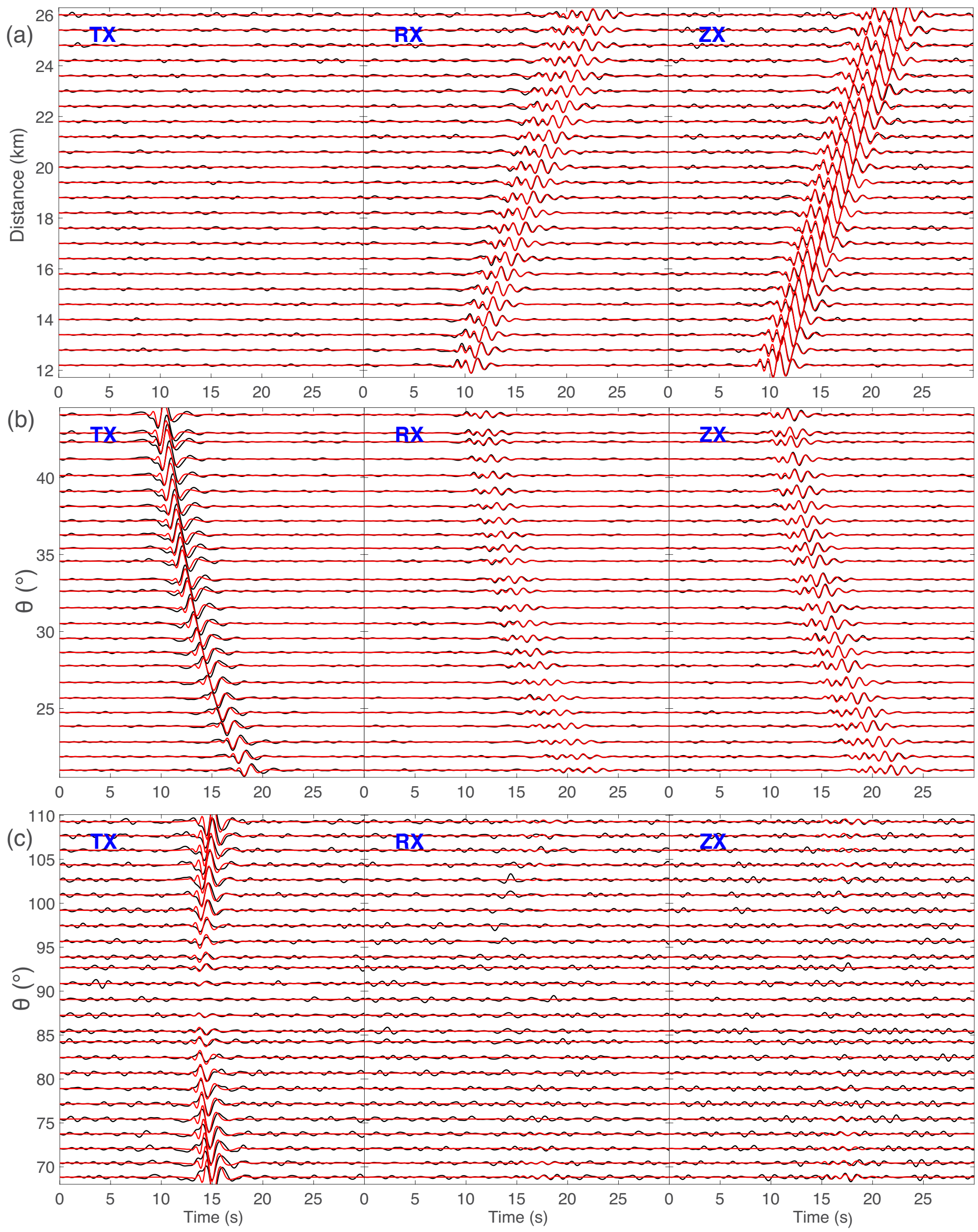

Figure 5. Figures showing comparisons of theoretical axial strain response to input single step forces (red waveforms) and waveforms retrieved from noise cross-correlation (black) of synthetic velocity noise recorded at a three-component seismometer acting as a virtual source and synthetic axial strain-rate noise recorded by channels of a DAS array acting as virtual receivers (Figure 4). (a), (b), and (c) are for sources marked 1, 3, and 7, respectively. The waveforms are arranged by distance in (a) with $\theta = 0°$, and by θ in (b) and (c). The waveforms are filtered at 0.4-1.0 Hz using a zero-phase Butterworth filter. The three columns correspond to TX, RX and ZX components (indicated at the top left corner). Similar plots for sources 2, 4 and 5 are shown in Figure S2.

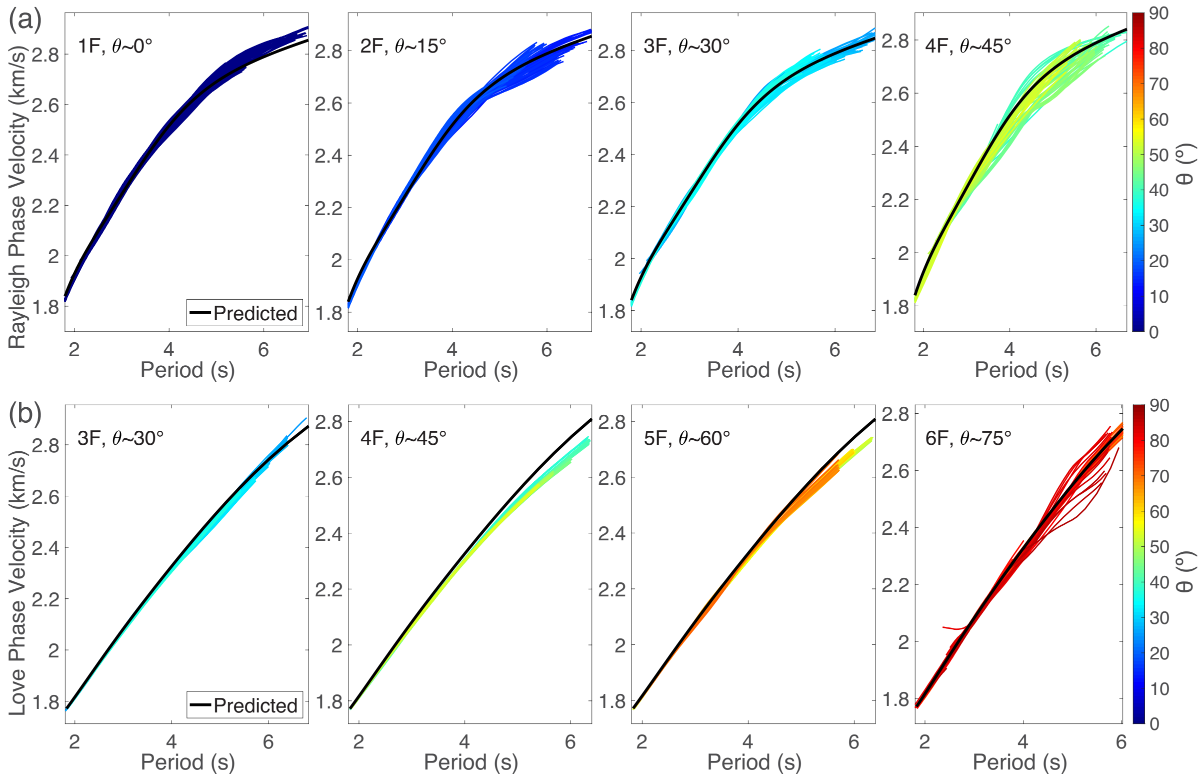

Figure 6. Phase velocity dispersion curves measured on the cross-correlations of synthetic noise (e.g. black waveforms shown in Figure 5). Plots in (a) and (b) show Rayleigh-wave and Love-wave dispersion measured on the ZX and TX components, respectively. Different plots are for different virtual sources (seismometers in the outer circle, Figure 4a); the source and the average θ are indicated on the top left corner. In each plot, the dispersion curves are for cross-correlations for the same seismometer with all channels of the DAS array, color-coded by θ ($\lesssim \pm 10°$ from the average value). The black curves are the predicted dispersion curves for the GIL7 model.

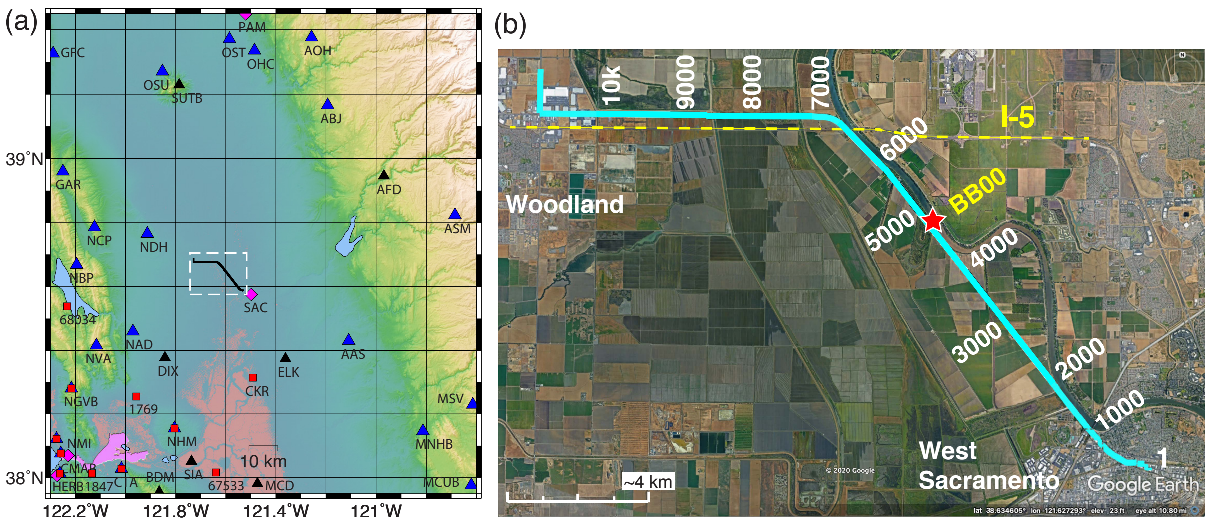

Figure 7. Map of the study area. (a) The solid black curve is the Lawrence Berkeley National Laboratory distributed acoustic sensing (DAS) array at Sacramento. Other symbols are permanent seismic stations (names indicated) – black triangle (broadband sensor), magenta diamond (three-component short-period sensor), blue triangle (vertical component short-period sensor), and red square (accelerometer). Some short-period sensors and accelerometers are installed in boreholes. The area marked by dashed white rectangle is expanded in panel (b). (b) In this Google Earth image, thick solid cyan line is the DAS array. Numbers in white indicate locations of specific channels for reference. Each 1000-channel cable segment is $\sim$2 km long. The location of the single broadband seismometer (BB00, red star), I-5 highway (dashed yellow line) and nearby cities are also marked.

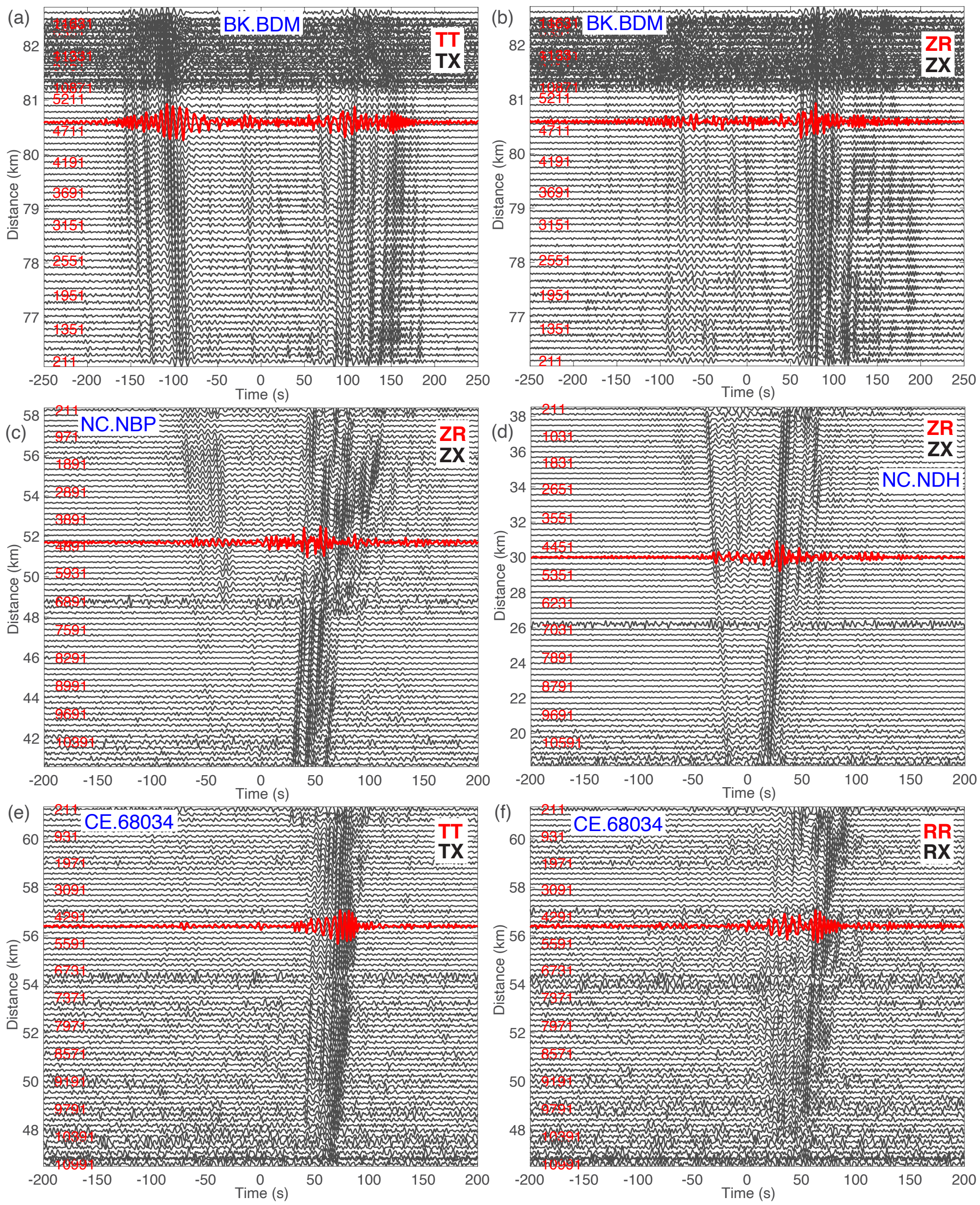

Figure 8. Each plot shows noise cross-correlation waveforms involving a specific regional permanent seismic station acting as the virtual source. The network and station name are indicated near the top of the plots in blue (format network.station). The gray waveforms are cross-correlations with channels of the DAS array arranged by distance. The red waveforms are cross-correlations with the temporary broadband station. The color-coded components corresponding to the two types of cross-correlations are indicated in the top right corner of each plot. Channel numbers for some channels of the DAS array (in red) are indicated next to the waveforms for reference. The type of sensors at the permanent stations are – broadband (BDM), vertical-component short-period (NBP and NDH), and accelerometer (68034). See Figure 7a for station locations.

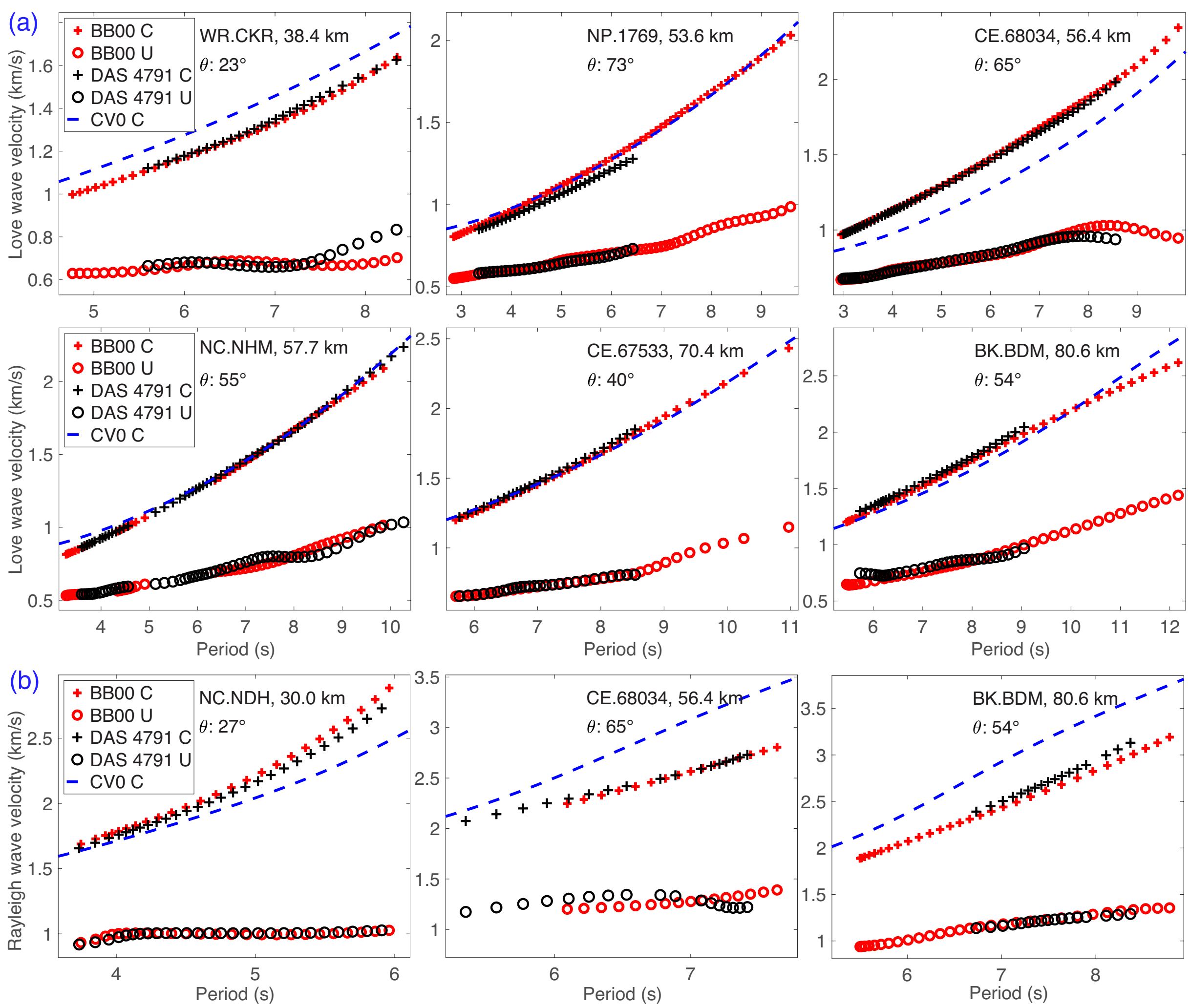

Figure 9. Comparison of surface-wave dispersion curves measured on seismometer-seismometer ("BB00", red) and seismometer-DAS ("DAS 4791", black) noise cross-correlations for the DAS channel (4791) closest to the temporary broadband seismometer. (a) Fundamental mode Love wave (b) 1st higher mode Rayleigh wave. Each plot is for a specific permanent seismic station acting as the virtual source – network and station name (format network.station), distance and the angle θ are indicated at the top of each plot. C: Phase velocity (+), U: Group Velocity (o). Dashed blue line is the reference dispersion curve. See Figure 7a for station locations.